DOE/BC/14899-26
Distribution Category UC-122

Visualization and Simulation of Immiscible Displacement in Fractured Systems Using Micromodels: Imbibition

By
Manouchehr Haghighi
Yanis C. Yortsos

July 1995

Work Performed Under Contract No. DE-FG22-93BC14899

Prepared for
U.S. Department of Energy
Assistant Secretary for Fossil Energy

Thomas B. Reid, Project Manager
Bartlesville Project Office
P.O. Box 1398
Bartlesville, OK 74005

Prepared by
University of Southern California
Petroleum Engineering Program
Department of Chemical Engineering
Los Angeles, CA 90089-1211

DISCLAIMER

DISCLAIMER

Portions of this document may be illegible in electronic image products. Images are produced from the best available original document.

Contents

List of Figures

ABSTRACT

A study of imbibition processes in micromodel geometries that mimic a matrix-fracture system was undertaken. Experiments in glass micromodels and pore network simulation were conducted.

It was observed that, at low capillary number values the wetting fluid preferentially invaded the matrix. Two critical capillary numbers were identified, one for the start of penetration in the fracture when the viscosity ratio was much less than one, and another for which the rate of propagation of the front in the fracture is the same with that in the matrix, when the viscosity ratio was greater than one. These critical capillary numbers were well matched with the results of a pore network simulation. We also developed a simplified theory for both critical numbers. Free imbibition in fractured system was investigated and compared favorably with pore network simulation. This process first involves the rapid invasion of the matrix, followed by the subsequent penetration of the fracture.

1 Introduction

Steam injection is a potentially effective method for the recovery of heavy oil from reservoirs. There are large accumulation of heavy crude and tar sands subject to steam injection in certain parts of the world, especially in western Canada, central Venezuela and in California and Utah in U.S.[18]. Steam injection can also be used to recover light crude much more effectively than waterflooding [18]. Naturally fractured reservoir may contain 25-30% of the world supply of oil [20]. Thus, steam injection in fractured reservoirs has a high potential importance in oil production.

Unfortunately, the understanding of steam injection in fractured systems is currently based mostly on phenomenology and typically consists of applying a double porosity formalism to steam simulators [4] [11] [14]. Most of these simulators use capillary imbibition as a mechanism for the exchange of fluids between the matrix blocks and the fracture network. Such a purely numerical approach offers little to further our insight into the process. A reasonable alternative is to conduct experiments in model geometries that mimic fractured systems. Glass micromodels can be constructed to mimic there. In this research, steam injection experiments in these models was conducted.

Since steam is non-wetting when in the vapor phase, but becomes wetting when condensed, steam injection involves both drainage and imbibition mechanisms in addition to the temperature effects on displacement and phase change. Therefore, to understand its effects the mechanisms isothermal displacement in fractured systems must first be studied. For this, based on visualization experiments we developed theories for both drainage and imbibition. A pore network simulator was also used to compare the experimental results and confirm the theory. Previously, we reported results on drainage processes [8]. In this report, we shall present our findings on imbibition. Steam displacement will reported in future reports.

1.1 Literature Review on Immiscible Displacement in Fractured Systems

Immiscible displacement in disordered porous media proceeds by different mechanisms, depending on the nature and history of the displacement (drainage or imbibition, primary or secondary process). These mechanisms have been clearly elucidated in recent years, notably by Lenormand who conducted careful experimental studies in micromodel geometries [15]. The local displacement

mechanics are not expected to change when a fracture-matrix system is considered. Thus, primary displacements will proceed by a frontal advance of the menisci, the conditions for which vary depending on whether the process is drainage or imbibition, the latter including the possibility of flow along the surface roughness. Secondary imbibition will involve in addition film flow, film thickening and snap-off, resulting at low rates in displacements different than frontal. In a fracture-matrix system, or in a system containing a streak of high permeability, the presence of fractures (or high permeability streaks) adds an element of large-scale correlation. These large scale features affect the composite process and introduce important flow rate effects.

Mattax and Kyte [17] who studied imbibition in fractured water-drive reservoirs, experimented with a single matrix block and studied the effect of the matrix block size to predict the recovery behavior for a reservoir matrix block from an imbibition test on a core sample. They introduced the following scaling equation

$$t_d = t\sqrt{\frac{k}{\phi}}[\frac{\sigma}{\mu_w L^2}] \tag{1}$$

They also introduced the concept of a "critical rate", in connection with water advance in fractured-matrix reservoirs. This was defined as the rate for which the water advance level in the fracture is the same to the water level in the matrix. For rates less than the critical, the water level in the matrix is above that in the fractures. Thus, all the recoverable oil will be displaced from the matrix block before the water in the fractures reaches the top of the block. Inversely, at rates greater than the critical, the water level in the fracture moves ahead of the water in the matrix and the matrix block is completely surrounded by water before imbibition is completed.

Eka and Ershaghi [7] considered gas injection in naturally fractured reservoirs. This process was simulated using a mathematical model that included both gravity and capillarity forces. They concluded that recovery of oil from low permeability matrix block can be improved by temporarily shutting in production wells when the gas-oil ratios are high. Labastie [13] discussed the capillary continuity between the matrix blocks during the gravity drainage in fractured reservoirs. He showed both experimentally and numerically that the oil recovery by a gravity drainage process in a naturally fractured reservoir strongly depends on the total height and capillary continuity. Rossen and Shen [19] proposed pseudo-capillary pressure curves for both the matrix and fracture to represent gravity drainage mechanism, which they used in a dual porosity simulator.

In theoretical studies on displacements in fractured systems, the main emphasis has been on

deriving some representation of the matrix imbibition rate, either by solving an appropriate initial boundary value problem or by introducing various simplifying assumptions. For example, Aronofsky et al. [1] defined a simple exponential relation between recovery and time for a single matrix block due to water invasion in fractured reservoirs. de Swaan [6] presented a theory in which the matrix blocks downstream are exposed to a varying water saturation resulting from the water imbibition upstream blocks. He used as a convolution integral a solution in terms of a known solution with a unit-step boundary condition proposed by Aronofsky et al. [1].

In the first visualization study in fractured systems, Handy and Datta [10] provided visual evidence of water imbibing in an artificially-fractured sandstones and in a heterogeneous sand pack. In the case of fractured sandstone, they observed that the water moves preferentially through the fracture, due to the low capillary pressure, while in the heterogeneous sand pack water imbibes into the fine sand because of capillary forces stronger than in the coarse sand. As rates increased, the water was seen to move preferentially through the more permeable regions. Handy [9] proposed a rate equation for imbibition and discussed the validity of the use of the diffusion equation with a nonlinear diffusion coefficient as a model for imbibition. Babadagli [2] conducted a series of forced imbibition experiments in model fractured sandstones, visualized by CT scanning, which demonstrated that effective relative permeabilities of the composite system (fracture and matrix) are strong functions of flow rate and the properties of the matrix and fracture, such as matrix permeability and fracture aperture.

2 Imbibition

Imbibition is among the processes that may be involved in steam displacement in fractured systems. Imbibition mechanisms in the presence of fractures have not adequately been studied in the past. Previous work was concentrated on experiments with core or on simulation using a double porosity simulator. Notably lacking are flow visualization using transparent 2-D micromodels and simulation of the matrix-fracture interaction. In this chapter, our objective is to provide a better insight on the recovery mechanisms in fractured systems during forced and free imbibition (both primary and secondary). To achieve this goal, pore level and larger scale visualization were first performed in a glass micromodel of a fracture-like structure, and a parametric experimental study of the effects

of capillary number, mobility ratio, and gravity was undertaken. Next, we developed a simplified theory to predict the observed mechanisms. Subsequently, a pore network simulation of primary and secondary imbibition was used in order to compare the experimental results with the numerical output, and provide more details of the process.

2.1 Experiments

The experimental set-up in this chapter is the same as that for drainage. We used both triangular and square pattern micromodels. The values of the network and fracture parameters are shown in Table 1.

Table 1: Micromodel characteristics

Network	Square	Triangular
Length	11.2 cm	12.5 cm
Width	5.7 cm	7.5 cm
Number of squares	51×26	75×45
Maximum bond width	0.1 cm	0.04 cm
Minimum bond width	0.04 cm	0.04 cm
Average bond width	0.07 cm	0.04 cm
Fracture width	0.2 cm	0.2 cm
Fracture depth	0.018 cm	0.01 cm
Network depth	0.009 cm	0.01 cm

Forced experiments were carried out at constant rate by the use of a syringe pump. A video camera with a close-up kit provided the desired visualization. The front movement were also recorded under a microscope for clearer visualization. The following four fluid pairs were used in the experiments:

1. Distilled water-air.

2. Distilled water-kerosene.

3. Distilled water-heavy mineral oil.

4. Distilled water-Dutrex 2621 (a synthetic oil, product of Shell Company with a measured viscosity of 10000 cP at 25°C).

In all experiments, kerosene and mineral oil were dyed with Fat Red 7B, and water was dyed with either Methylene Blue or Fluorescein. We used the measured value of 70 dynes/cm for the interfacial tension of water-air, and the approximate value of 35 dynes/cm for all water-oil systems.

2.2 Forced Primary Imbibition

Primary imbibition is the displacement of a non-wetting fluid by a wetting fluid in the absence of prewetting. Systematic primary imbibition experiments were carried out for each fluid pair at four different capillary numbers (Table 2).

In this set of experiments, we used the micromodel with triangular pore pattern, of coordination number 6. It was found that in experiments with water displacing air, and for a capillary number 2×10^{-6} and lower, the water invaded the matrix first. At the pore level, both in the inlet of the model and in the matrix, two different and simultaneous mechanisms were clearly observed: 1- Water flow along the roughness of the walls (Figures 1-6); 2- Meniscus movement (Figures 7-9). The flow of water along the surface roughness causes accumulation of water on the walls (Figures 1 and 2). With sufficient accumulation on one wall only, the radius of curvature of the interface increases, until it touches the opposite wall pore and the adjacent channel is invaded instantaneously. When there is sufficient accumulation of water on walls, only the channel is filled. At capillary numbers below 2×10^{-8}, both mechanisms were at work (Figure 3 and 4), resulting into a rough-shaped front (Figure 5). However, at capillary numbers above 2×10^{-7}, only the first mechanism was operating and no channel filling was observed; thus, the water invaded the network in a frontal movement that proceed line-by-line (Figure 6). Both these mechanisms are in agreement with earlier studies [15]. At the capillary number of 2×10^{-5}, water invaded the fracture at the same time that invaded the matrix. In this regime, we observed meniscus movement only during which the viscous forces dominate the capillary forces. It follows, therefore, that a critical capillary number exists, where viscous forces are equal to capillary forces. In such cases, fracture and matrix are invaded at the same time. In our experiment, this critical capillary number lies between 2×10^{-5} and 2×10^{-6} for water-air system (Figure 7).

While the water-air experiments showed indeed that the wetting phase preferentially invades the

Table 2: Conditions for forced primary imbibition experiments

Fluid Pair	Displacing Fluid Viscosity (cP)	Mobility Ratio	Volumetric Rate (cc/min)	Capillary Number
Water-Air	1	0.018	0.00052	2×10^{-8}
"	"	"	0.0052	2×10^{-7}
"	"	"	0.052	2×10^{-6}
"	"	"	0.52	2×10^{-5}
Water-Kerosene	1	"	0.00052	4×10^{-8}
"	"	1.50	0.0052	4×10^{-7}
"	"	"	0.052	4×10^{-6}
"	"	"	0.52	4×10^{-5}
Water-Mineral oil	1	100	0.00052	4×10^{-8}
"	"	"	0.0052	4×10^{-7}
"	"	"	0.052	4×10^{-6}
"	"	"	0.52	4×10^{-5}
Water-Dutrex	1	10000	0.00052	4×10^{-8}
"	"	"	0.0052	4×10^{-7}
"	"	"	0.052	4×10^{-6}
"	"	"	0.52	4×10^{-5}

matrix block, this was not observed for a water-oil primary imbibition. At a capillary number lower than 4×10^{-6}, only the fracture was invaded. At higher values of the capillary number, water started to also invade the matrix similarly to drainage processes. Figures 8 and 9 show water-kerosene and water-Dutrex at a capillary number of 4×10^{-6}. At these experiments, water moves through the fracture only. We believe that this is due to the change of wettability in the micromodel. When the glass is first exposed to it, the micromodel is contaminated with polar compounds existing in oil [5]. These components tend to adsorb on the micromodel roughness and render them oil-wet and the process turns out to be like drainage. For future work, it is recommended, as a solution of this problem, to use non-oil fluids such as air-mercury, or to perform imbibition tests using an oil-wet model.

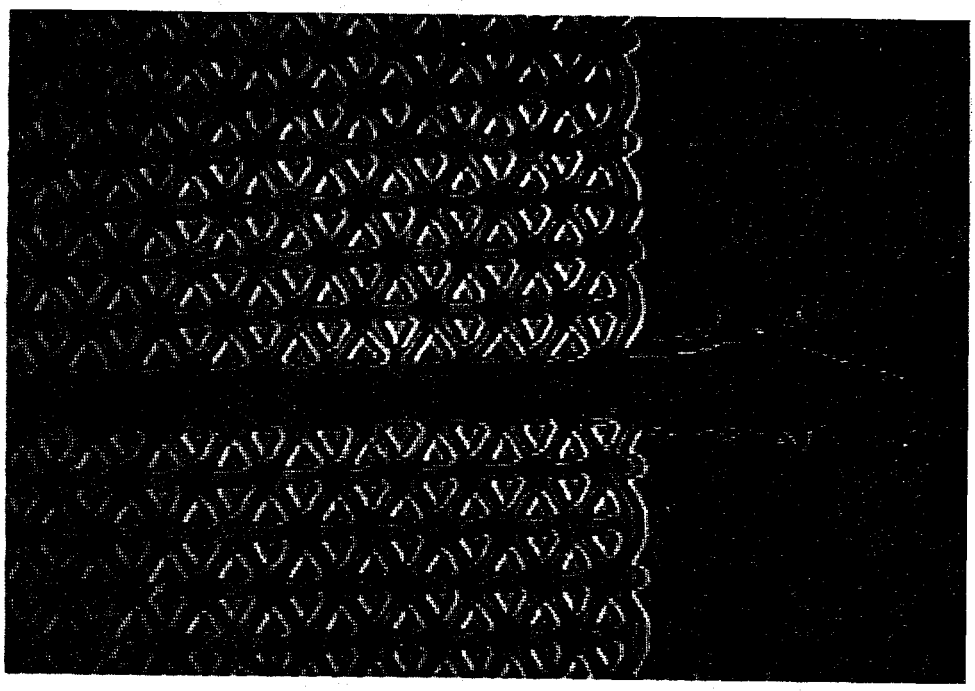

Figure 1: Primary imbibition (water-air) showing roughness flow.

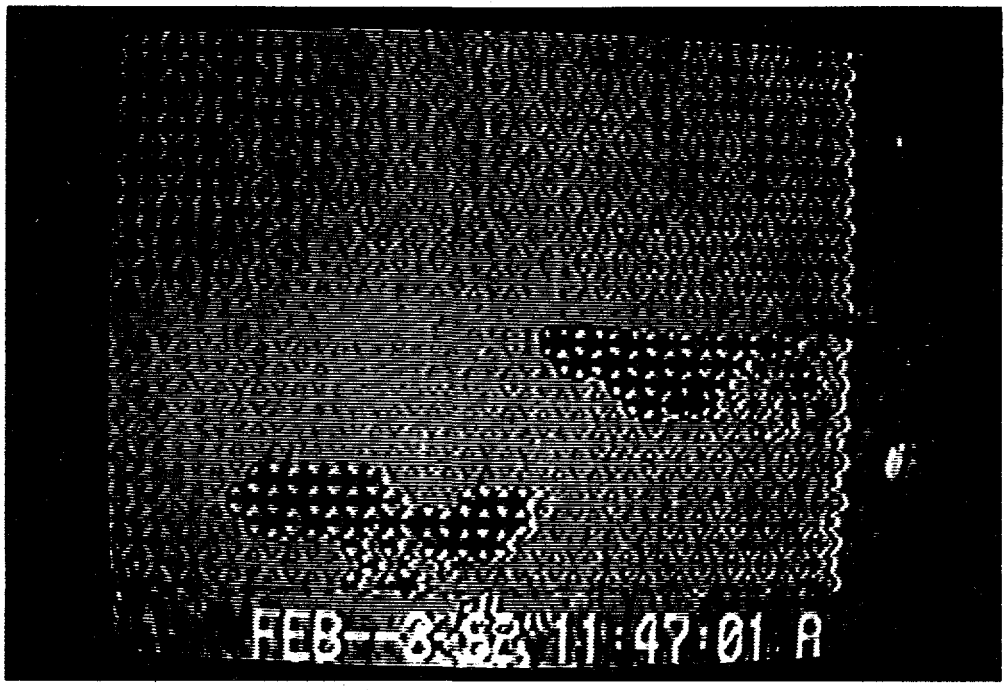

Figure 2: Primary imbibition (water-air) $Ca = 2 \times 10^{-8}$, showing discontinuous invasion of the model through roughness flow.

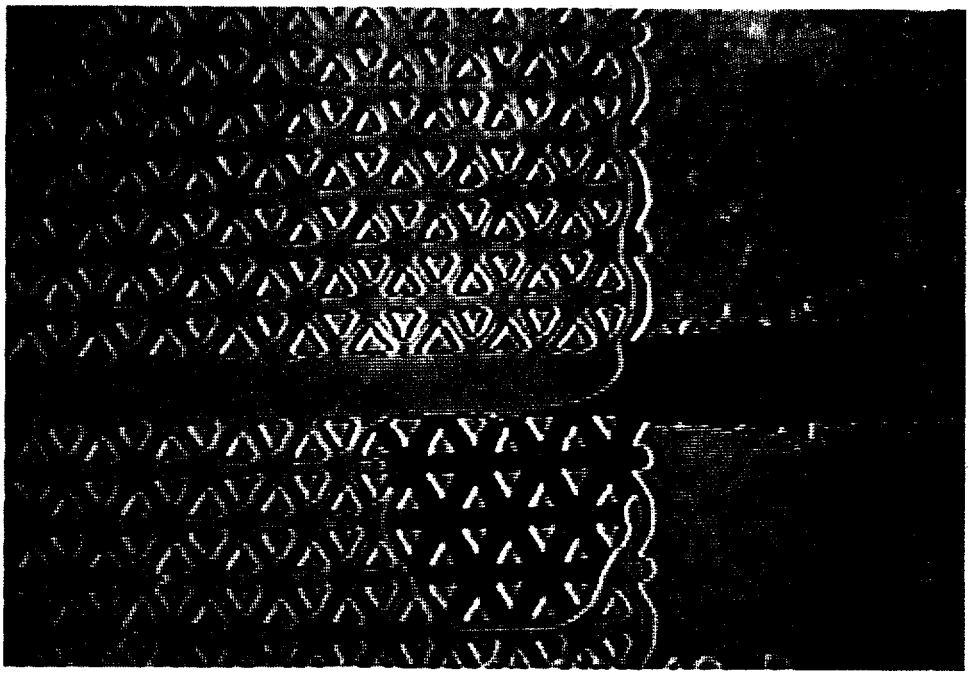

Figure 3: Primary imbibition (water-air) at $Ca = 2 \times 10^{-8}$, showing both pore invasion and channel filling (snapshot 1).

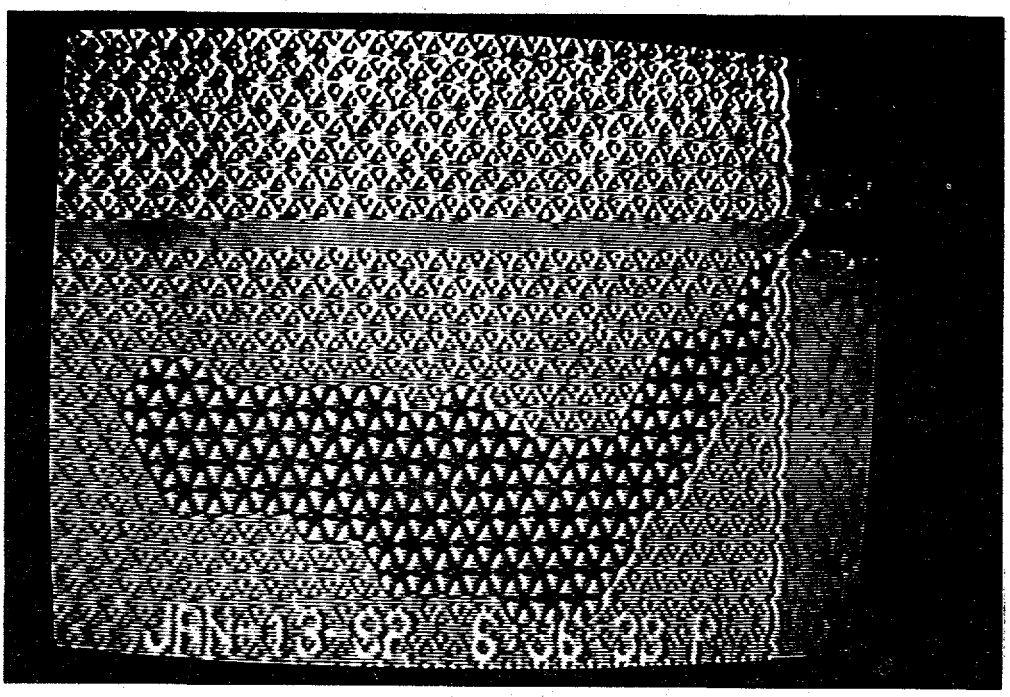

Figure 4: Primary imbibition (water-air) at $Ca = 2 \times 10^{-8}$, showing both pore invasion and channel filling (snapshot 2).

Figure 5: Primary imbibition (water-air) at $Ca = 2 \times 10^{-8}$ (snapshot 3).

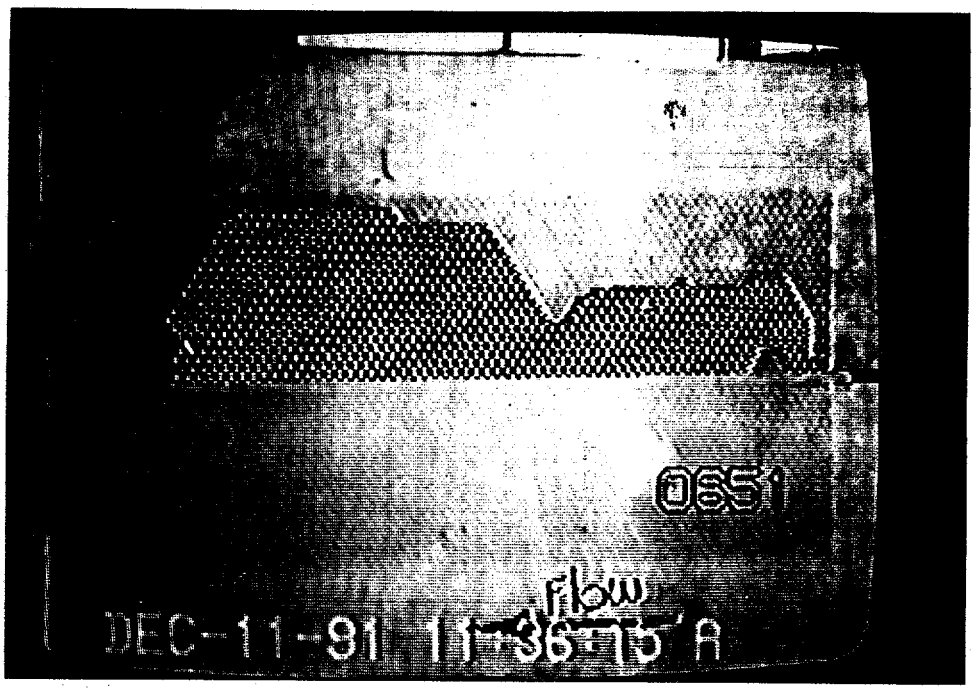

Figure 6: Primary imbibition (water-air) at $Ca = 2 \times 10^{-7}$.

Figure 7: Primary imbibition (water-air) at $Ca = 2 \times 10^{-5}$, showing simultaneous invasion of the fracture and the matrix.

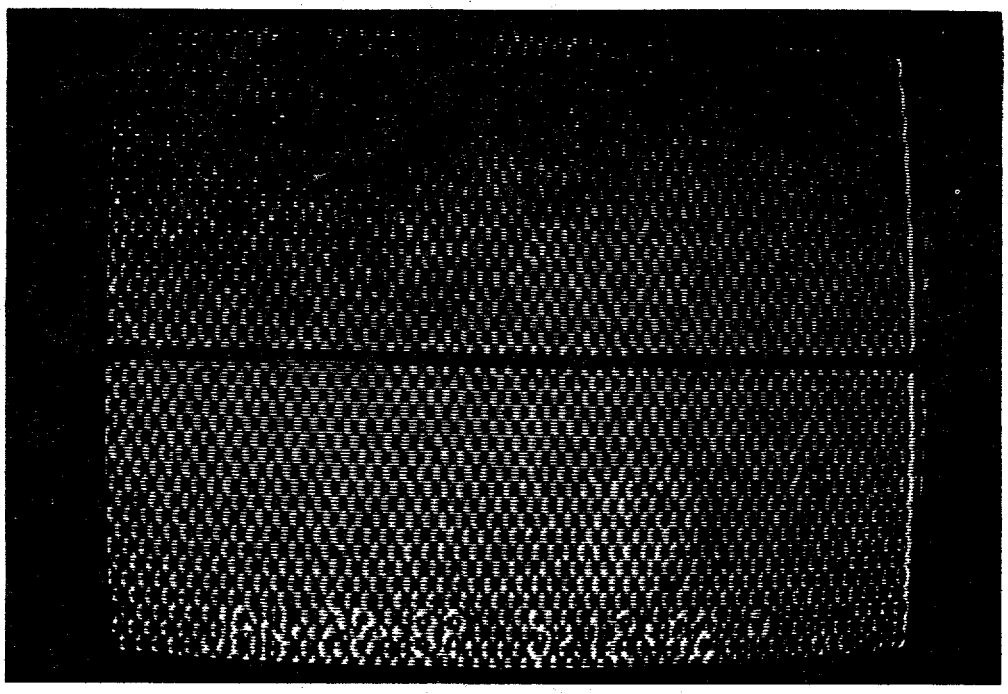

Figure 8: Primary imbibition (water-kerosene) at $Ca = 4 \times 10^{-6}$, showing that water moves through the fracture only.

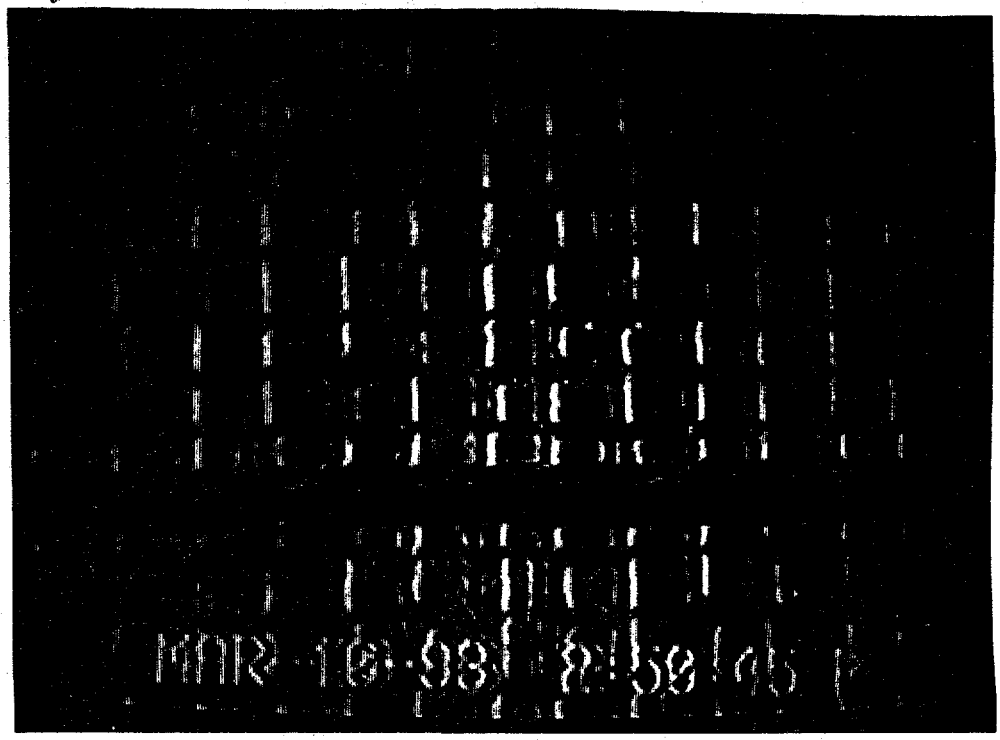

Figure 9: Close-up of primary imbibition (water-Dutrex) at $Ca = 4 \times 10^{-6}$, showing that water moves through the fracture only.

2.3 Secondary Forced Imbibition

Next, we considered secondary imbibition, in which the wettability was preserved by preventing any oil contact with the surface of the micromodel because of prewetted conditions. In secondary imbibition, the model was first saturated with water. Then, the non-wetting phase was injected at capillary number values greater than 10^{-5} (in excess of the critical value) in order to displace most of the wetting phase. This regime causes the least amount of trapping although trapped wetting phase still remains. Obviously, the precise way drainage has taken place substantially affect the subsequent mechanism of secondary imbibition. This set of experiments pertained to an initial drainage at relatively high capillary numbers. Here, the resulting residual water films were not interconnected. This has significant effects on the secondary imbibition. Table 3 shows the various parameter values used in the different runs.

During the experiments involving the fluid pair water-air, water invades the matrix block following a mechanism different than for the case of primary imbibition. Now, the displacement is a succession of rapid invasion jumps that occur along the existing water films, left behind at the conclusion of primary drainage (Figures 10 and 11). This mechanism operates at low capillary numbers. At higher values, the typical meniscus displacement of the previous process was also observed.

For the experiments involving the fluid pair water-kerosene, a secondary imbibition mechanism similar to the water-air system was observed at the capillary number 4×10^{-6} (Figures 12 and 13). Water was found to enter the fracture first. Then, the matrix block was invaded with a chain of rapid jumps as soon as the injecting water started to communicate with the previous water film along the roughness of the network. Oil was trapped in the pores, while adjacent channels were occupied with water at the conclusion of the snap-off process. At capillary number values lower than 10^{-6} this mechanism was not observed. Rather all water were found to enter the fracture first, and then pores adjacent to the fracture started to be invaded slowly (Figures 14 and 15). We attribute this lack of spontaneous imbibition to the lack of connectivity between the residual water films.

In the experiments with heavy oil, where the mobility ratio was higher than 100, water moves to the fracture first. However, before water breakthrough in the fracture, it also invaded the matrix. We will analyze this process later in theory section. The mechanism of displacement both in the

Table 3: Conditions for secondary imbibition experiments

Fluid Pair	Displacing Fluid Viscosity (cP)	Mobility Ratio	Volumetric Rate (cc/min)	Capillary Number
Water-Air	1	0.018	0.00052	2×10^{-8}
"	"	"	0.0052	2×10^{-7}
"	"	"	0.052	2×10^{-6}
"	"	"	0.52	2×10^{-5}
Water-Kerosene	1	"	0.00052	4×10^{-8}
"	"	1.50	0.0052	4×10^{-7}
"	"	"	0.052	4×10^{-6}
"	"	"	0.52	4×10^{-5}
Water-Mineral oil	1	100	0.00052	4×10^{-8}
"	"	"	0.0052	4×10^{-7}
"	"	"	0.052	4×10^{-6}
"	"	"	0.52	4×10^{-5}
Water-Dutrex 2621	1	10000	0.00052	4×10^{-8}
"	"	"	0.0052	4×10^{-7}
"	"	"	0.052	4×10^{-6}
"	"	"	0.52	4×10^{-5}

pore throat and in the fracture is a slow, uniform meniscus movement. In these experiments, we observed that if a relatively heavy oil is used for drainage, the water film left behind is apparently very thin, such that spontaneous imbibition will not take place. However, as it is shown in Figures (16-19), secondary imbibition is a very slow process. For example, in water displacing heavy mineral oil, the complete imbibition requires about 100 pore volumes of water injection. Also, as shown in Figures 17-19, because of the slowness of the process, at lower capillary numbers, we experience a higher displacement efficiency.

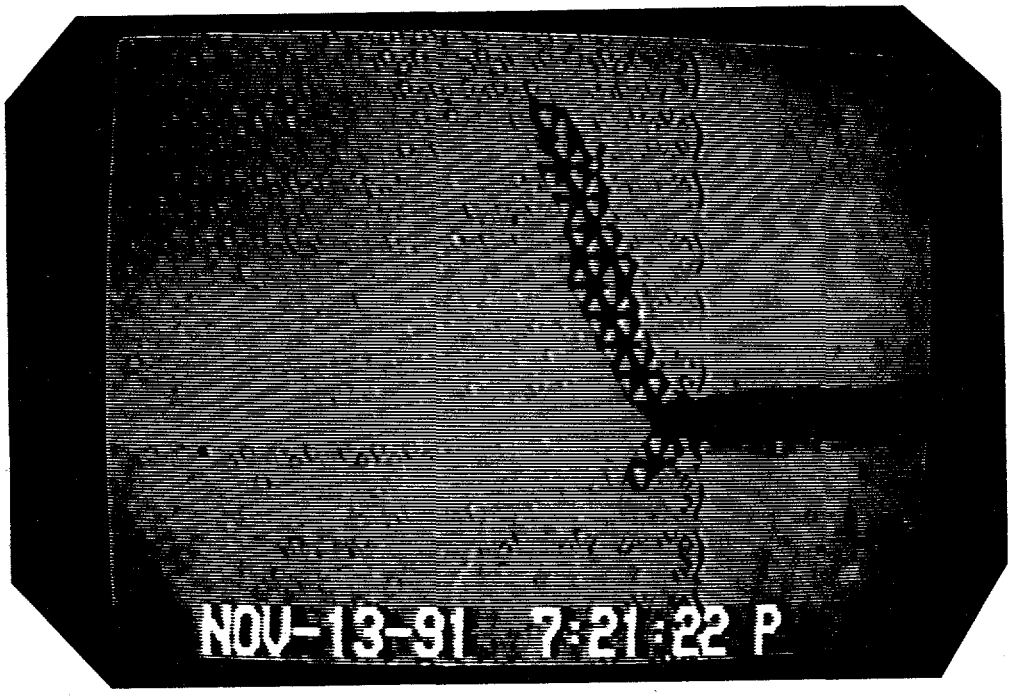

Figure 10: Secondary imbibition (water-air) at $Ca = 2 \times 10^{-8}$ (snapshot 1).

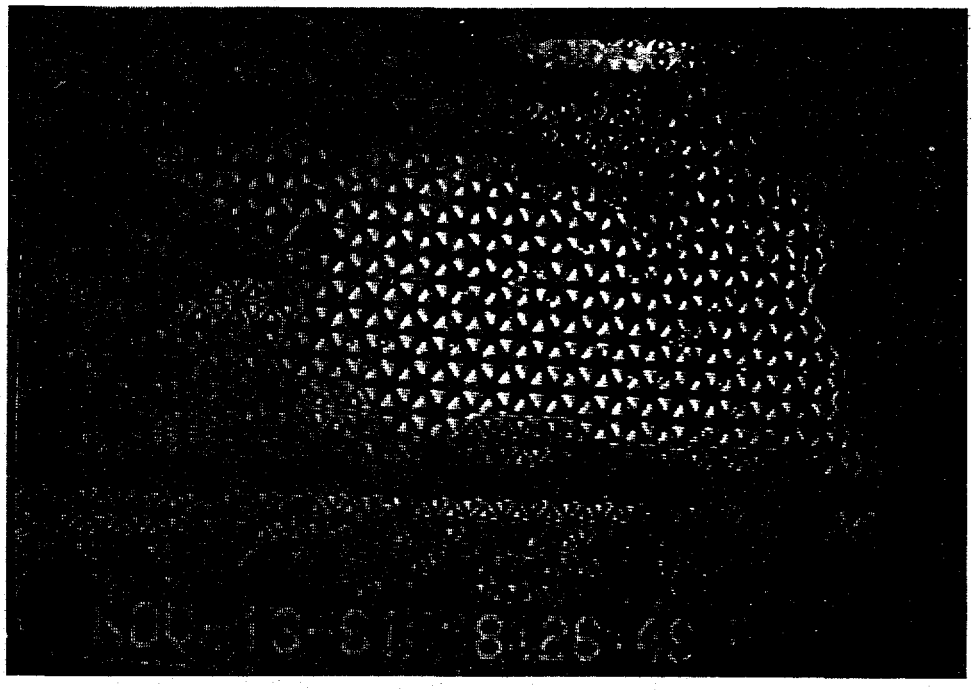

Figure 11: Secondary imbibition (water-air) at $Ca = 2 \times 10^{-8}$ (snapshot 2).

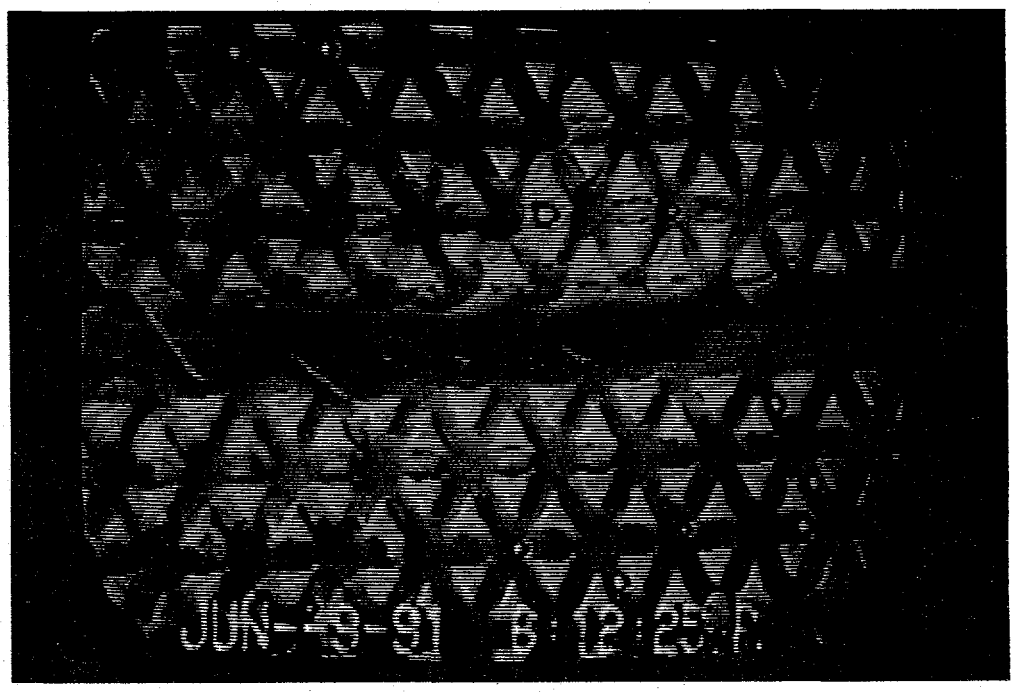

Figure 12: Secondary imbibition (water-kerosene) at $Ca = 4 \times 10^{-6}$ (snapshot 1).

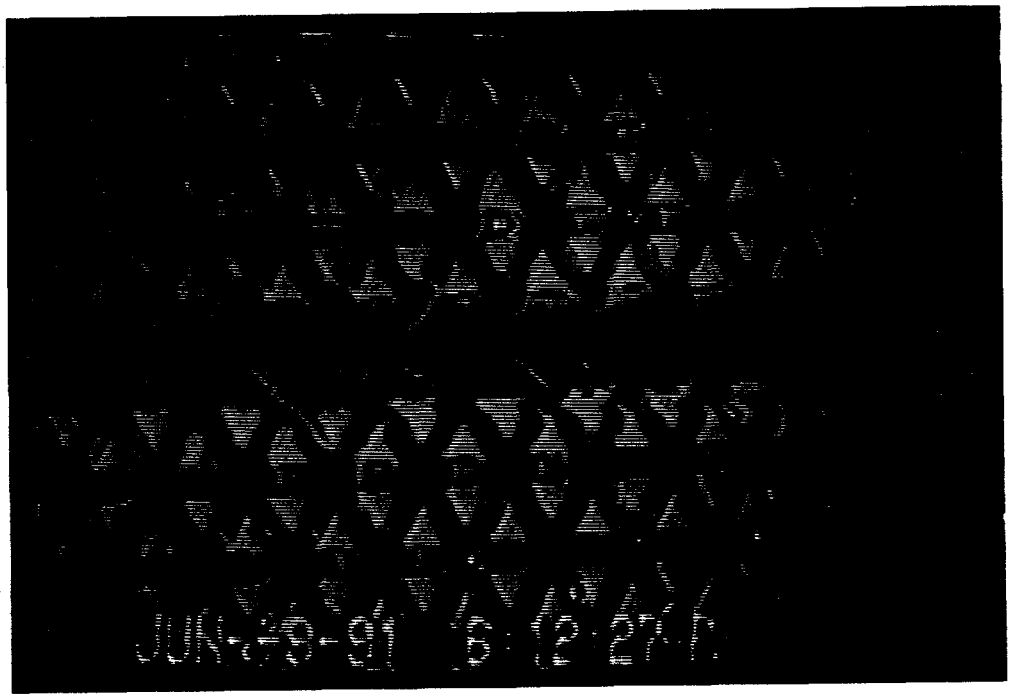

Figure 13: Secondary imbibition (water-kerosene) at $Ca = 4 \times 10^{-6}$ (snapshot 2).

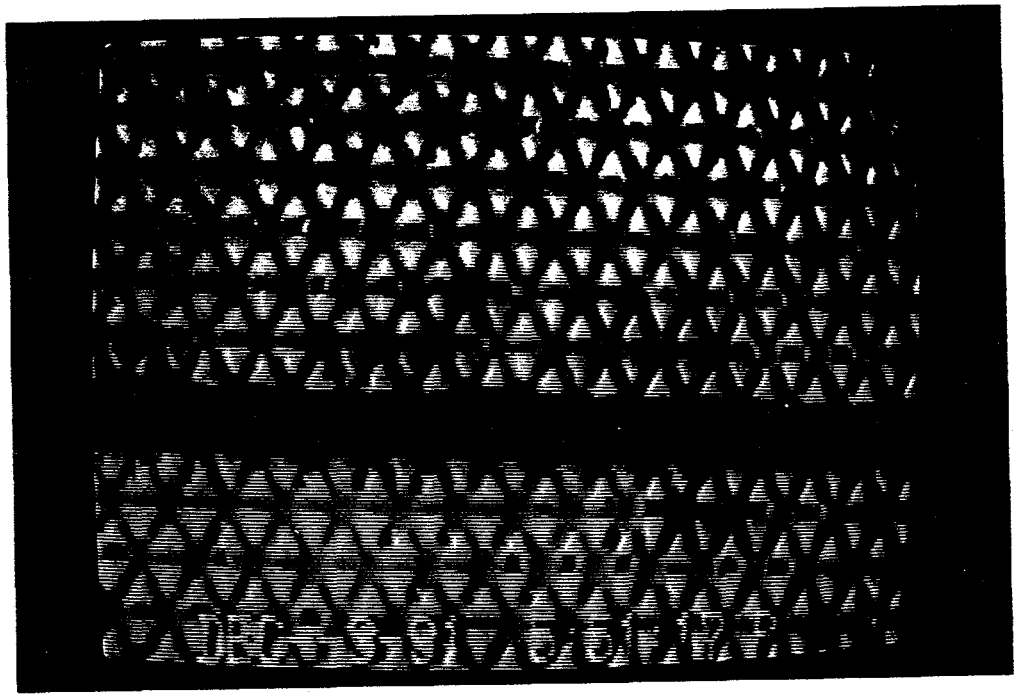

Figure 14: Secondary imbibition (water-kerosene) at $Ca = 4 \times 10^{-7}$.

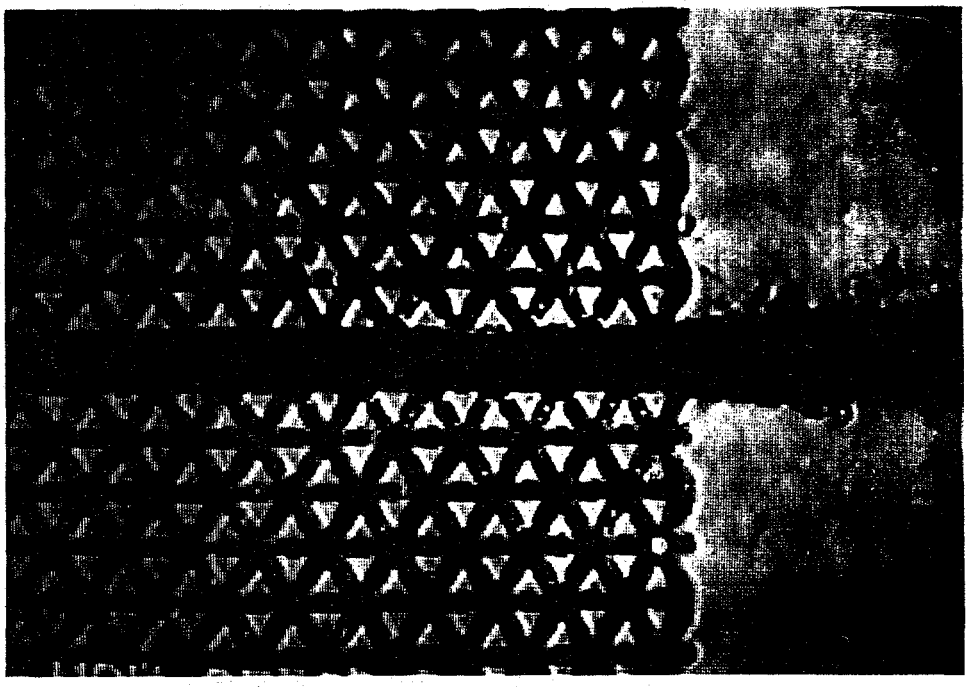

Figure 15: Secondary imbibition (water-kerosene) at $Ca = 4 \times 10^{-8}$.

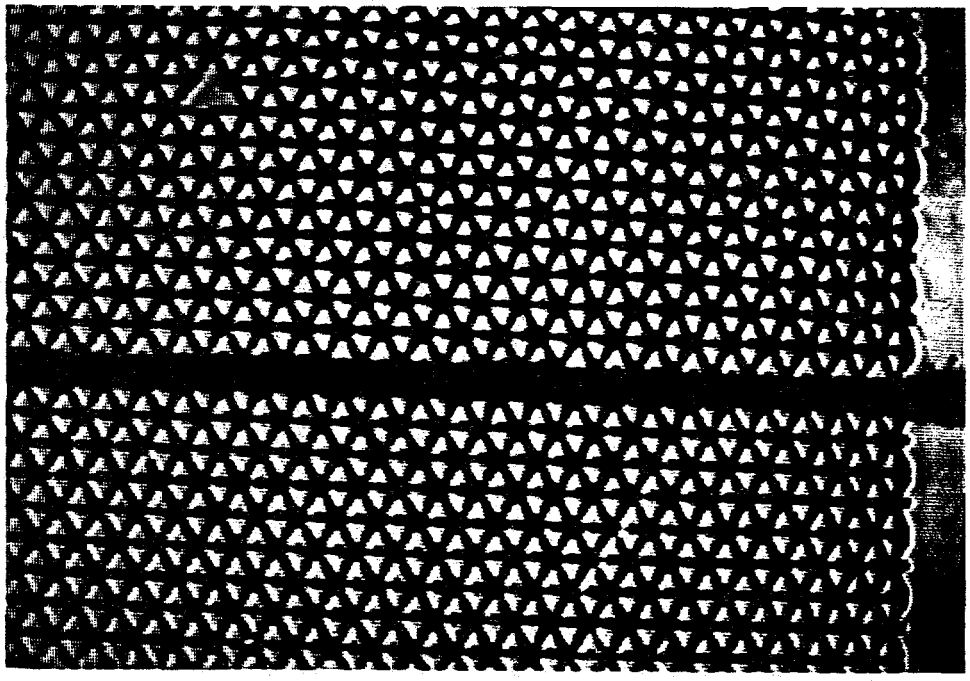

Figure 16: Secondary imbibition (water-heavy oil) at $Ca = 4 \times 10^{-8}$.

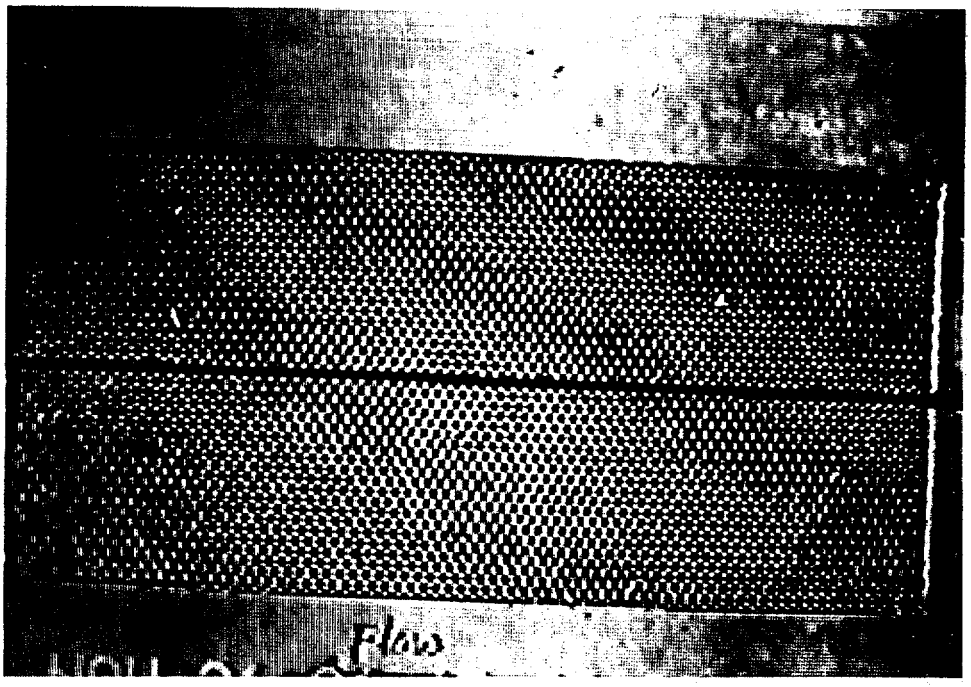

Figure 17: Secondary imbibition (water-heavy oil) at $Ca = 4 \times 10^{-7}$.

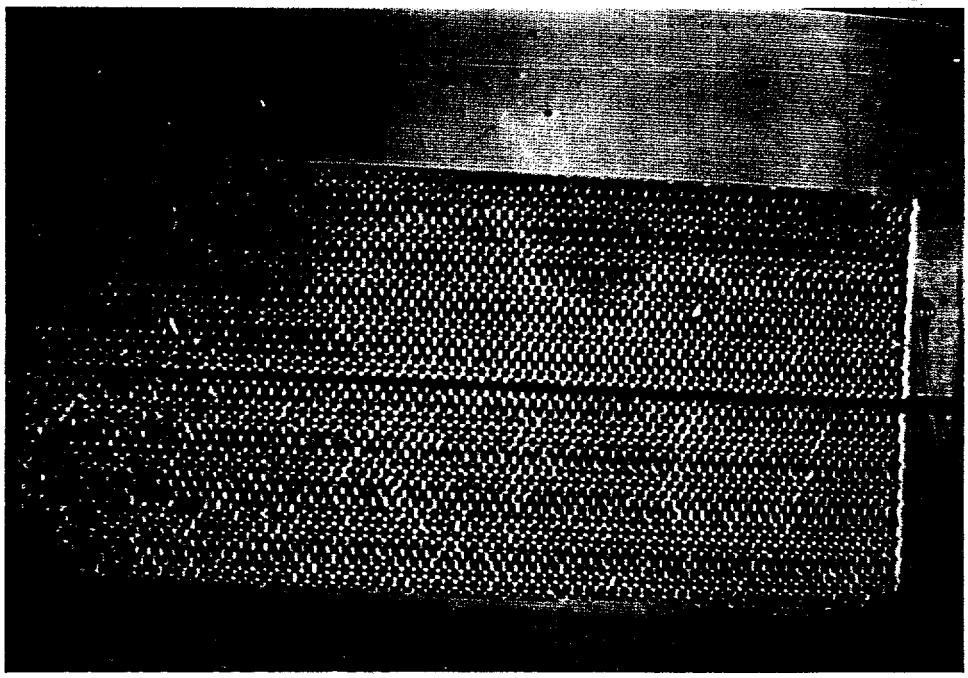

Figure 18: Secondary imbibition (water-heavy oil) at $Ca = 4 \times 10^{-6}$.

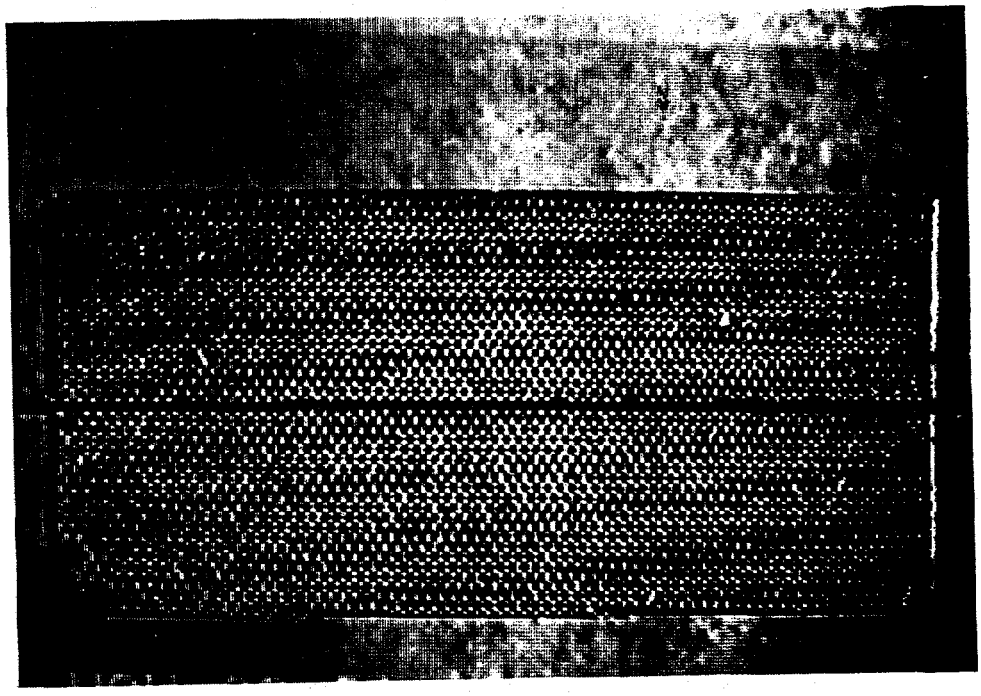

Figure 19: Secondary imbibition (water-heavy oil) at $Ca = 4 \times 10^{-5}$.

2.4 Free Imbibition

Free imbibition was experimented with water-air system. Dyed water was introduced into the clean and dry micromodel through a plastic tubing connected to a pipette. To prevent any gravity force resulting from the water column in the pipette at the beginning of the experiment, the plastic tubing was closed, and the water vertical level in pipette was balanced with the level of the micromodel. Then, the tubing was opened and water moved into the model. Since the inlet of the model is connected to the fracture, water movement was stopped at the inlet due to the capillarity of the fracture (Fig.20). Thus, it was necessary to raise the water level in the pipette by a few millimeters to provide a small gravity force to overcome the capillary pressure at the inlet and to start invasion into the network. After invasion started, the pipette was lowered to its original level. Water invaded the network by capillary forces only. The fracture was also invaded; however, the water front in the network was always a head of that in the fracture (Figures 21-23).

At the beginning, this test was observed to occur rapidly, but later it becomes a slow displacement. The mechanism is similar to the exponential decay of water saturation versus time proposed by Aronofsky et al. [1].

Later in this chapter, the numerical simulation of this process will be compared with experimental data.

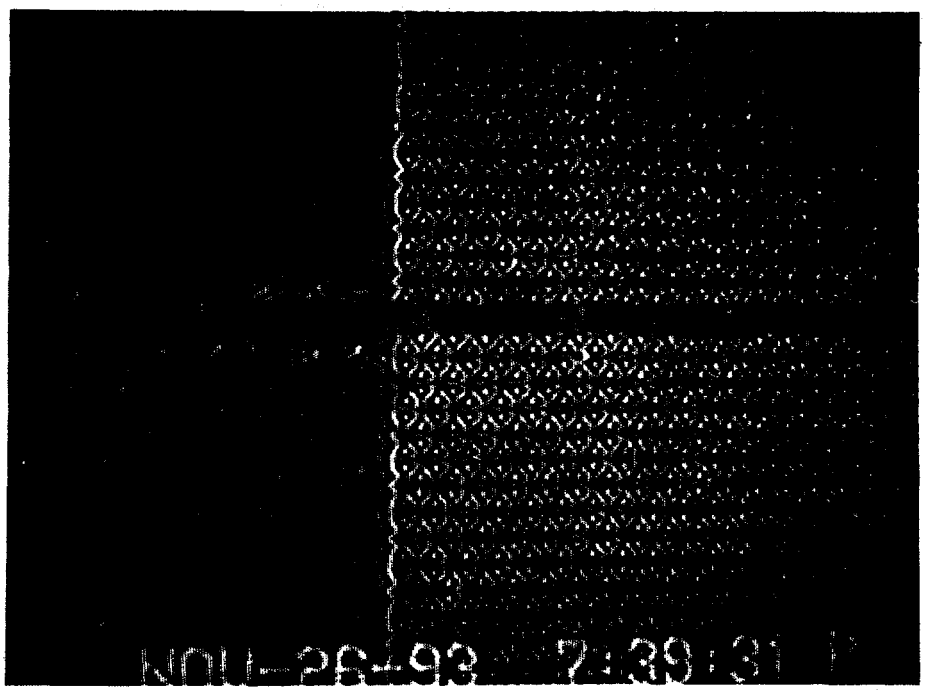

Figure 20: Free imbibition (water-air) (snapshot 1).

Figure 21: Free imbibition (water-air) (snapshot 2).

Figure 22: Free imbibition (water-air) (snapshot 3).

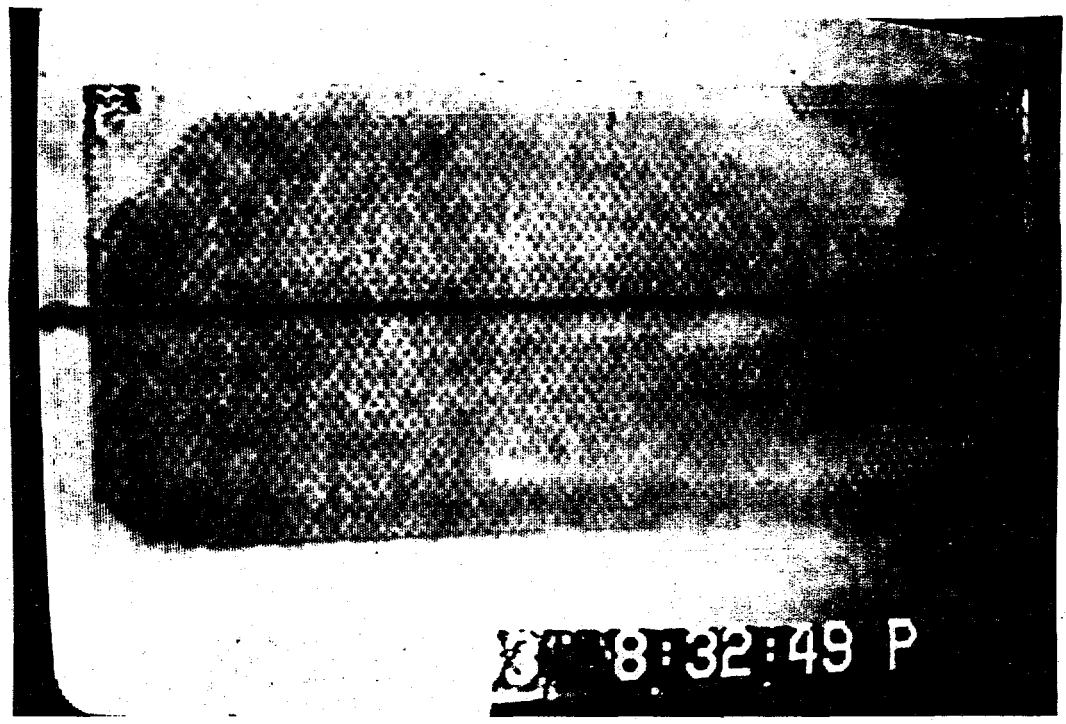

Figure 23: Free imbibition (water-air) (snapshot 4).

2.5 Gravity Effects

The next set of experiments investigated effects of gravity in water displacing kerosene following two different geometrical configurations, one with the micromodel tilted at a small angle with respect to horizontal, and another with the model rotated to the gravity vector (vertical cross-section). The water was not dyed in this set of experiments. All experiments were carried out at a capillary number of 4×10^{-6}.

In the first configuration we probed effects of formation dip. Water was injected from the bottom (updip) or from the top (downdip). For updip injection, a flat and stable displacement front with small size oil entrapments were observed (Figure 24). In contrast, for downdip injection, the density difference acted to destabilize the front resulting into an unstable fingering mechanism with large size oil entrapments (Figure 25). Fingers in the fracture was more developed than in the matrix.

In the second configuration we examined effects of gravity override. The injected water flowed downwards towards the bottom of the model. Figure 26 shows the process at steady state.

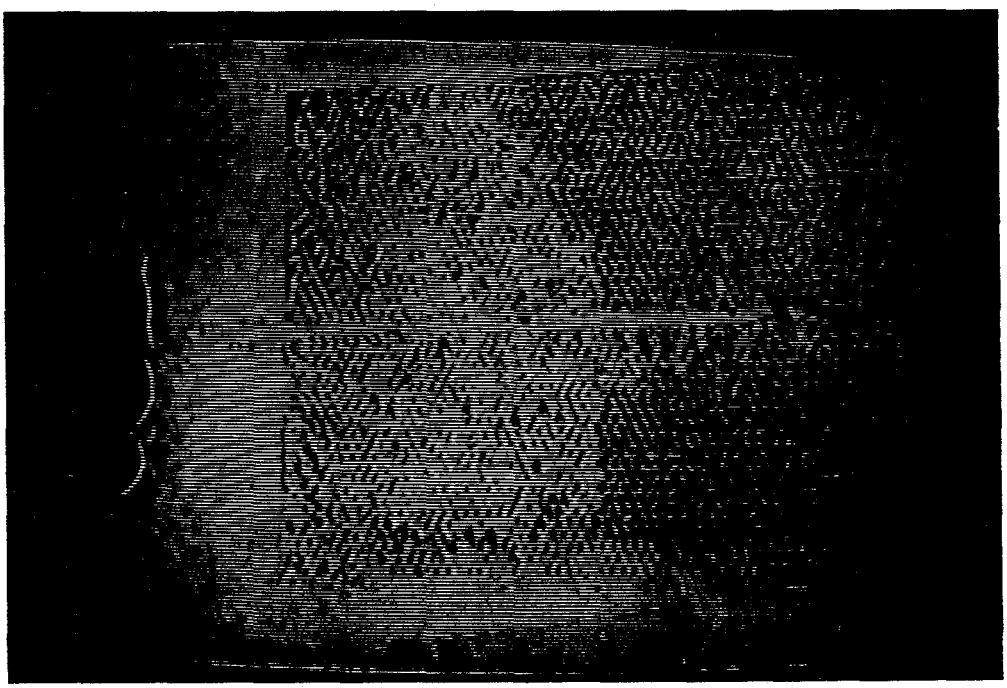

Figure 24: Updip water injection.

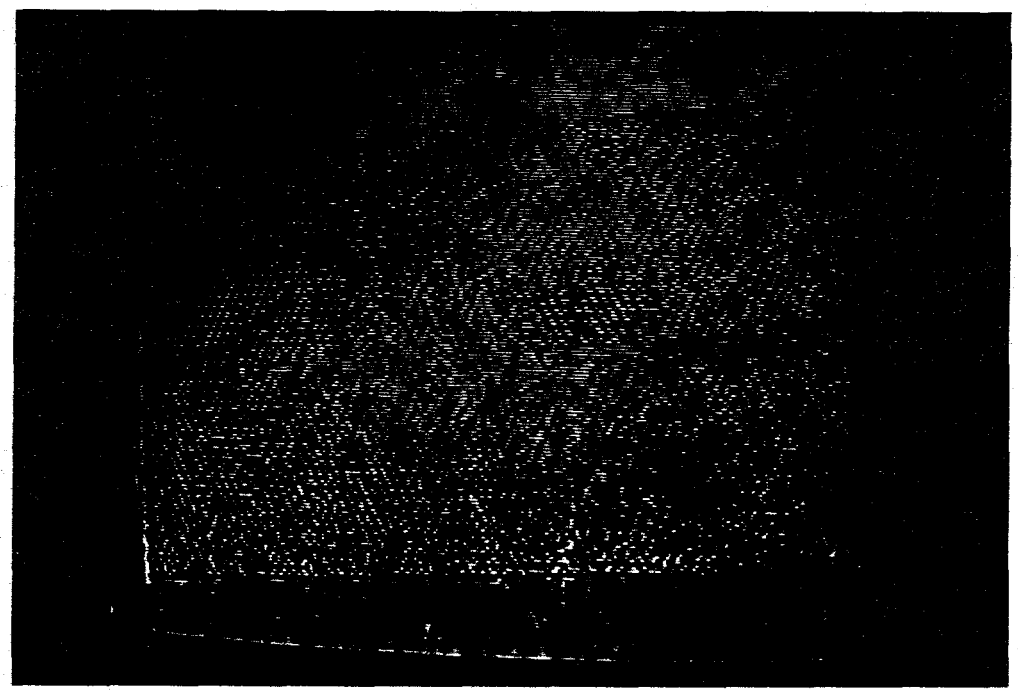

Figure 25: Downdip water injection.

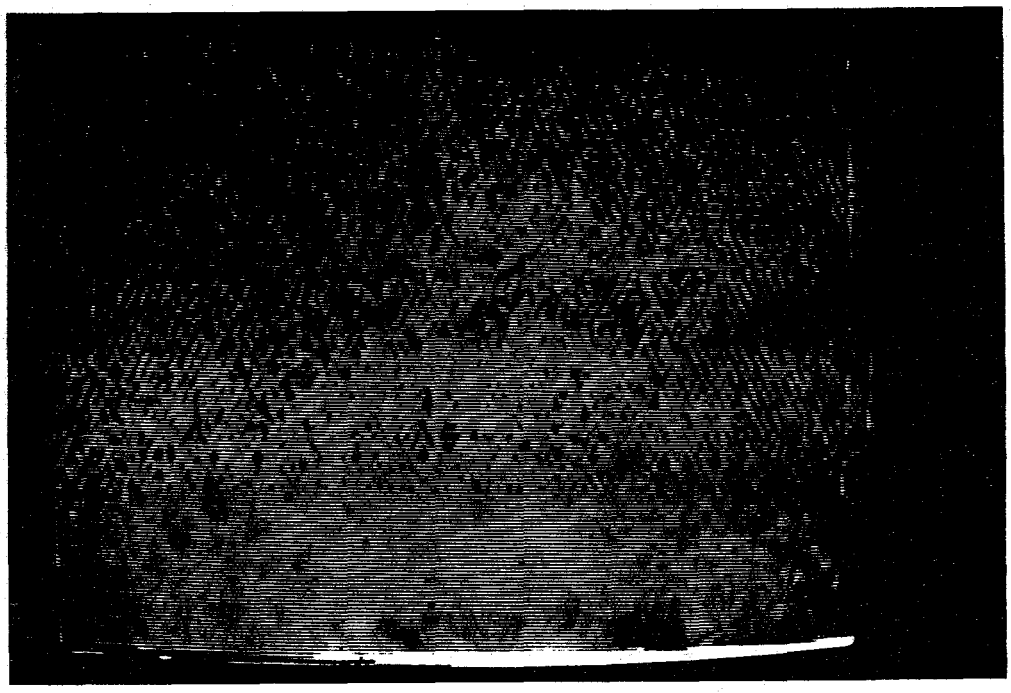

Figure 26: Water injection in a vertical cross-section.

3 Theory

In the previous section, we experimentally visualized forced primary imbibition with water displacing air (mobility ratio of 0.018). If the capillary number is sufficiently small, all injected fluid initially flows along the roughness of the walls of the pore network. At higher injection rates, the wetting fluid flows at the bulk of pore network without any fracture penetration. At higher rates, the fracture is also invaded, but the front in the network is ahead of that in the fracture. Finally, when the injection rate is raised above to a critical value, the front of the wetting fluid in the fracture travels faster than that of the network. For the case of water displacing oil at any capillary number, both fracture and matrix are invaded provided that the mobility ratio is greater than one. Therefore, it seems that there exist two critical capillary numbers, one for the start of penetration in the fracture and another for which the front of the wetting fluid in the fracture is the same to that in the matrix.

To calculate the first critical capillary number for the start of penetration in the fracture, the pressure drop at the inlet must be equal to the capillary pressure in the fracture (Fig. 27),

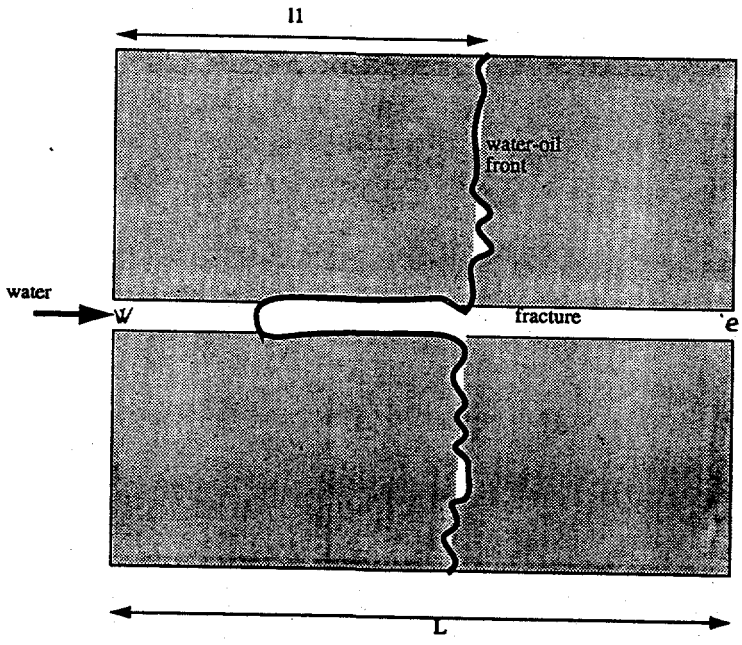

Figure 27: Schematic of fluids distribution after fracture penetration.

$$P_e - P_w = \frac{2\sigma}{r_f} \tag{2}$$

where σ is interfacial tension and r_f is the fracture radius. Application of Darcy's law for both wetting and non-wetting phases in the matrix gives

$$P_w - P_{wf} = \frac{q\mu_w l_1}{k_m k_{rw}} \tag{3}$$

and

$$P_{nwf} - P_e = \frac{q\mu_{nw}(L - l_1)}{k_m k_{rnw}} \tag{4}$$

where q is fluid velocity, μ is viscosity, k_m is matrix permeability, k_r is relative permeability and we used subscripts w, nw and f to denote wetting, non-wetting and front. In addition, at the displacement front in the network, the capillary pressure relationship exists

$$P_{wf} - P_{nwf} = -\frac{2\sigma}{r_m} \tag{5}$$

where r_m is the average pore radius of matrix. By combining equations (3), (4), (5) and substitution into the condition for the critical capillary number, $P_e - P_w = \frac{2\sigma}{r_f}$, we obtain

$$2\sigma(\frac{1}{r_m} - \frac{1}{r_f}) = \frac{q}{k_m}[\frac{(L - l_1)\mu_{nw}}{k_{rnw}} + \frac{l_1\mu_w}{k_{rw}}]. \tag{6}$$

If, now, $M \ll 1$, μ_{nw} can be neglected compared to μ_w, and using the capillary number definition $Ca = \frac{q\mu}{\sigma}$, equation (6) gives the critical value

$$Ca^* = \frac{2k_m}{L}(\frac{1}{r_m} - \frac{1}{r_f}) \tag{7}$$

By assumption, r_f is much greater than r_m, thus $\frac{1}{r_f}$ can be neglected compared to $\frac{1}{r_m}$, hence

$$(Ca^*)_1 = \frac{2k_m}{Lr_m} \tag{8}$$

The same is true also for the case of arbitary M, but where penetration of the fracture occurs only after the front has reached the end of the block. Equation (8) suggests that for $M \ll 1$, the fracture penetration depends on the geometric properties of matrix, more permeable and shorter matrix block causing earlier fracture penetration for the same fluids and injection rate.

To calculate the critical capillary number for which the displacement front in the matrix is the same as that in the fracture, the pressure drop in the fracture should be equal to pressure drop in the matrix. The pressure drop in the matrix is

$$P_w - P_e = \frac{q\mu_w l}{k_m} + \frac{q\mu_{nw}(L-l)}{k_m} - \frac{2\sigma}{r_m} \tag{9}$$

while the pressure drop in the fracture is

$$P_w - P_e = \frac{q\mu_w l}{k_f} + \frac{q\mu_{nw}(L-l)}{k_f} - \frac{2\sigma}{r_f}. \tag{10}$$

At the entrance ($l = 0$) equating the right side of equations (9) and (10) gives

$$\frac{Lq\mu_{nw}}{\sigma} = \frac{2(\frac{1}{r_m} - \frac{1}{r_f})}{(\frac{1}{k_m} - \frac{1}{k_f})}. \tag{11}$$

By substitution of the capillary number $Ca = \frac{q\mu}{\sigma}$ and the viscosity ratio $M = \frac{\mu_{nw}}{\mu_w}$ into (11) and making the assumption that $\frac{1}{k_f}$ and $\frac{1}{r_f}$ can be neglected compared to $\frac{1}{k_m}$ and $\frac{1}{r_m}$, respectively, the second critical capillary number is obtained

$$(Ca^*)_2 = \frac{2k_m}{r_m ML} \tag{12}$$

This critical capillary number depends on the geometric properties of matrix *and* the viscosity ratio. For capillary number less than the above value, the wetting fluid front in the matrix is ahead of that in the fracture; inversely, at capillary numbers greater than the critical value, the wetting fluid moves ahead of the wetting fluid in the matrix. We compared the above critical capillary number with the Mattax and Kyte [17] experiments, where they carried out a water-drive on a fracture-matrix system and found the critical rate to be $3''/day$. Their experiment was performed on a 1.9-md sandstone with a porosity of 9.1 percent, viscosity of water 0.9 cP, viscosity of oil 2.7 cP, and interfacial tension of 35 $dynes/cm$. The length of the sample was 3 inches. Based on the above data, the capillary number is calculated to be 2.3×10^{-8}. The critical capillary number from equation (12) using the Katz and Thompson formula [12] for the permeability calculation is computed to be 0.5×10^{-8}. Although both numbers are of the same order of magnitude, we should note that in deriving the theoretical formula, gravity was not considered, while in the Mattax and Kyte experiment, water was injected at the bottom of the sample. Thus, the actual capillary number is higher than the theoretical. Comparison of the theoretical expressions with our network simulation and the micromodel experiments are discussed in the following section.

4 Simulation

To compare experimental and theoretical results with a numerical simulation, we used two different pore network simulation for imbibition developed by Xu in Ref. [3]; one for primary imbibition which does not consider film flow or snap-off mechanisms, and another for secondary imbibition which accounts for film flow and snap-off which are two mechanisms that occur in secondary imbibition. In the absence of film flow, simulation of imbibition is similar to drainage with the exception that the capillary pressure is calculated based on the pore instead of the bond radius, and the condition for invading the adjacent bond is $p_i + p_{cij} > p_j$, where p_{cij} is the capillary pressure between adjacent bonds i and j. We recall that the corresponding condition for drainage is $p_i > p_{cij} + p_j$. We used both constant flow rate and constant pressure boundary conditions. With a constant flow rate boundary, we were able to compare the numerical simulation with the forced primary imbibition experiments. With the constant pressure boundary, free imbibition can be simulated. In simulation of imbibition with film flow, which simulates secondary imbibition, Xu in Ref. [3] modified the conditions used by Lenormand et al. [16]. The pressure field is calculated based on Poiseuille's law using an SOR method for both the bulk zone and the film region. According to Lenormand et al. [16], when there is corner flow in non-circular cross-section channel, an unstable state of interface is reached when the meniscus at the two adjacent corners join and snap-off occurs. For a rectangular throat with side x and y, snap-off will happen when $p_c = \frac{2\sigma}{r}, (r = min(x, y))$. In our simulation, it is assumed that snap-off develops when the film covers the circle, in a condition similar to a square shape throat. For pore filling Lenormand et al. [16] categorized $Z - 1$ mechanisms for a network with a coordination number Z. For example, they defined mechanism $I1$ as that when pore is surrounded by $Z - 1$ filled bonds, $I2$ when a pore is surrounded by $Z - 2$ filled bonds, etc.. The pore filling conditions for the circular bonds and spherical pores are as follows:

$$p_{I1} = p_{nw} - p_w = \frac{2\sigma}{r_p} \tag{13}$$

and

$$p_{I2} = p_{nw} - p_w = \sigma(\frac{0.15}{r_t} + \frac{1}{r_p}) \tag{14}$$

Only one event occurs based on the pressure condition at any time step. If more than one event can happen, the pore which takes less time, first starts to fill and the time step increment is set

accordingly. At high flow rates, the rate of fluid injected into the system is more than that by which films can absorb; therefore, a frontal drive will prevail, similar to drainage. Further details on the simulator are available in [21].

We first run the simulator to simulate forced imbibition (absence of film flow) with the same pore structure and flow parameters used in the experiments. The simulations with the results from the corresponding experiments are shown in Figures 28-30. In this set, we used the square pattern micromodel in order to compare experiment with network simulations.

Figure 28 shows water displacing air in the micromodel and corresponding simulations for a capillary number of 1.8×10^{-5}. In this experiment, water moves only in the matrix and no penetration in the fracture is observed (the corresponding capillary number is below the critical capillary number for the start of penetration in the fracture). The network simulations of the experiment show that except for a few pores, the fracture is also not penetrated, and a generally good match with the experiments is obtained. In Figure 29, the water injection rate is increased to a capillary number of 5.4×10^{-5}. As shown on the left side of Figure 29, the fracture is now penetrated; however, the water front in the fracture is always behind the water front in the matrix. The simulation of this experiment, shown on the right side, also indicates fracture penetration as well. The critical capillary number for the start of invasion in the fracture was calculated to be 1.08×10^{-5}. From both simulation and experiment, this number must be between 1.8×10^{-5} and 5.4×10^{-5} which is of the same order of magnitude as the calculated. Figure 30 shows experiment and corresponding simulation for a capillary number of 5.4×10^{-4}. In this experiment, fracture and matrix were penetrated at the same time showing that the capillary number has exceeded its second critical value. Recall that the latter was defined as that dictating competition between the front in the fracture and that in the matrix, and for our experiment was calculated as 5.4×10^{-4}. The interactions between fracture and matrix in the experiment and the simulation were generally well matched. The critical capillary number derived is applicable both for experiments and simulations.

Subsequently, we run simulations for secondary imbibition namely by considering film flow and snap-off mechanisms. Figures 31-34 show the simulation results. In this set of figures, the left side shows the beginning of the process, the right side shows the steady state condition reached; invaded pores are shown with open circles, filled bonds following snap-off events are shown with dashes. First, we examined the low capillary number 5.4×10^{-8}. Film flow and snap-off are the

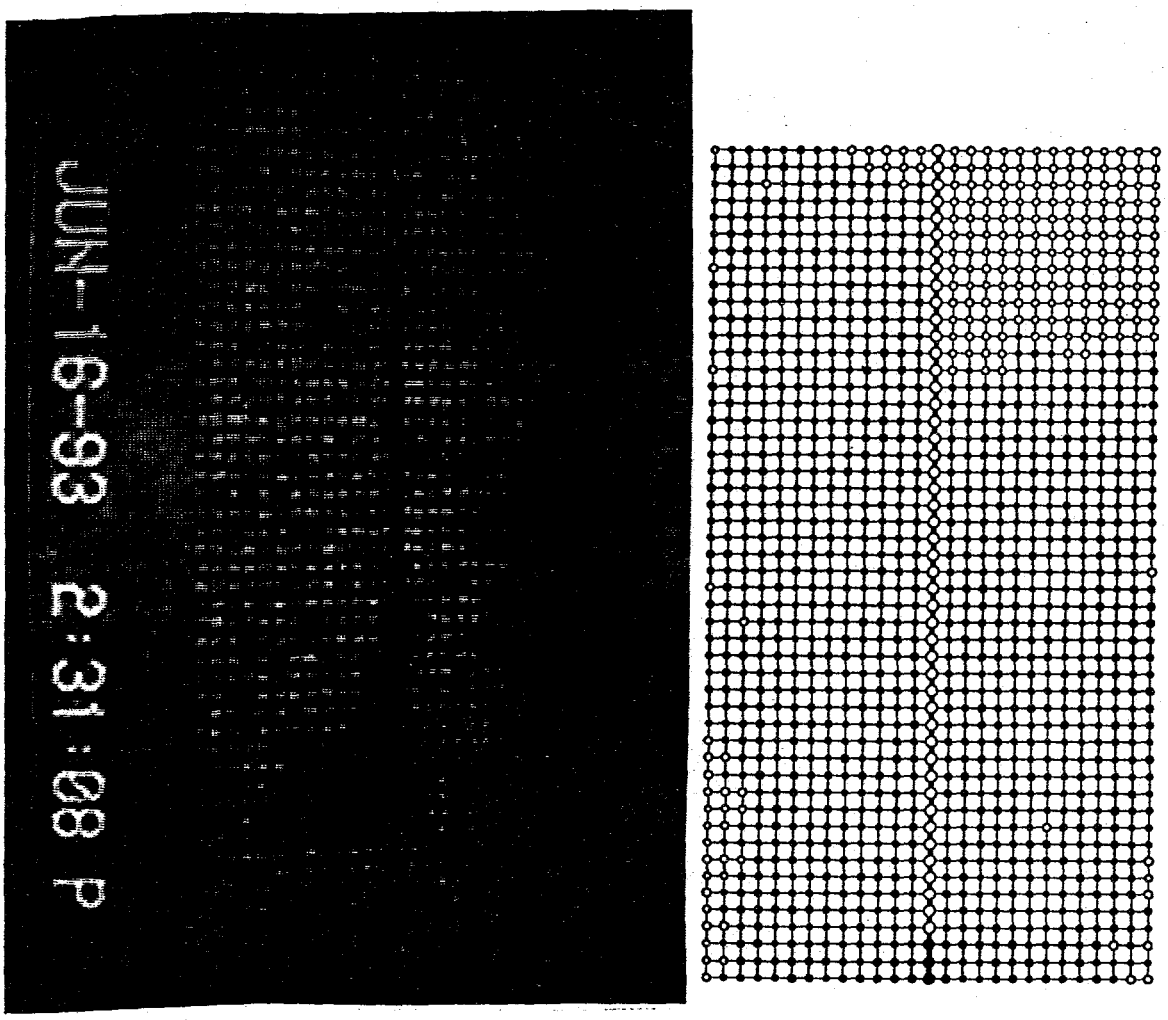

Figure 28: Comparison between experimental and numerical results for water-air, $Ca = 1.8 \times 10^{-5}$.

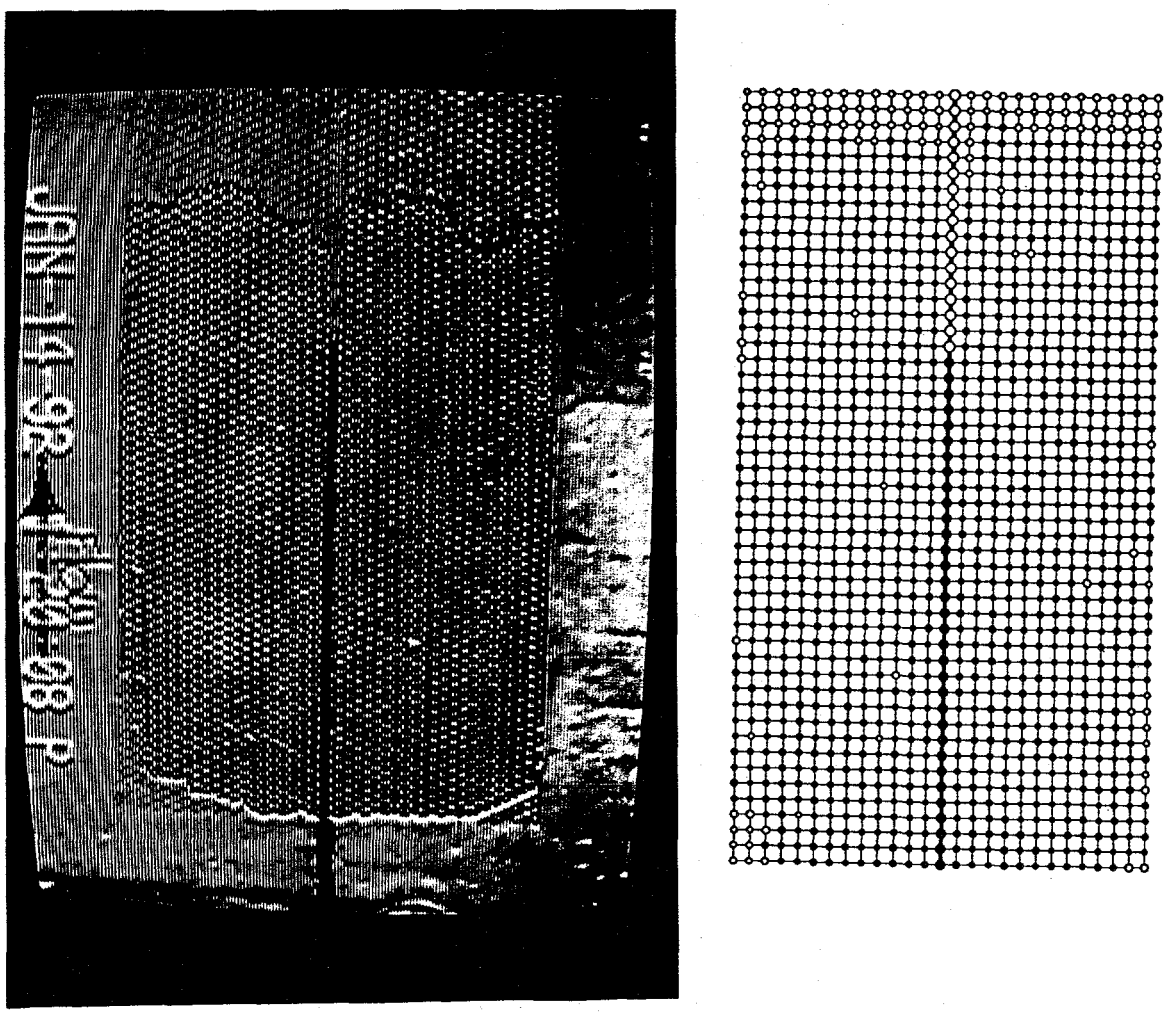

Figure 29: Comparison between experimental and numerical results for water-air, $Ca = 5.4 \times 10^{-5}$.

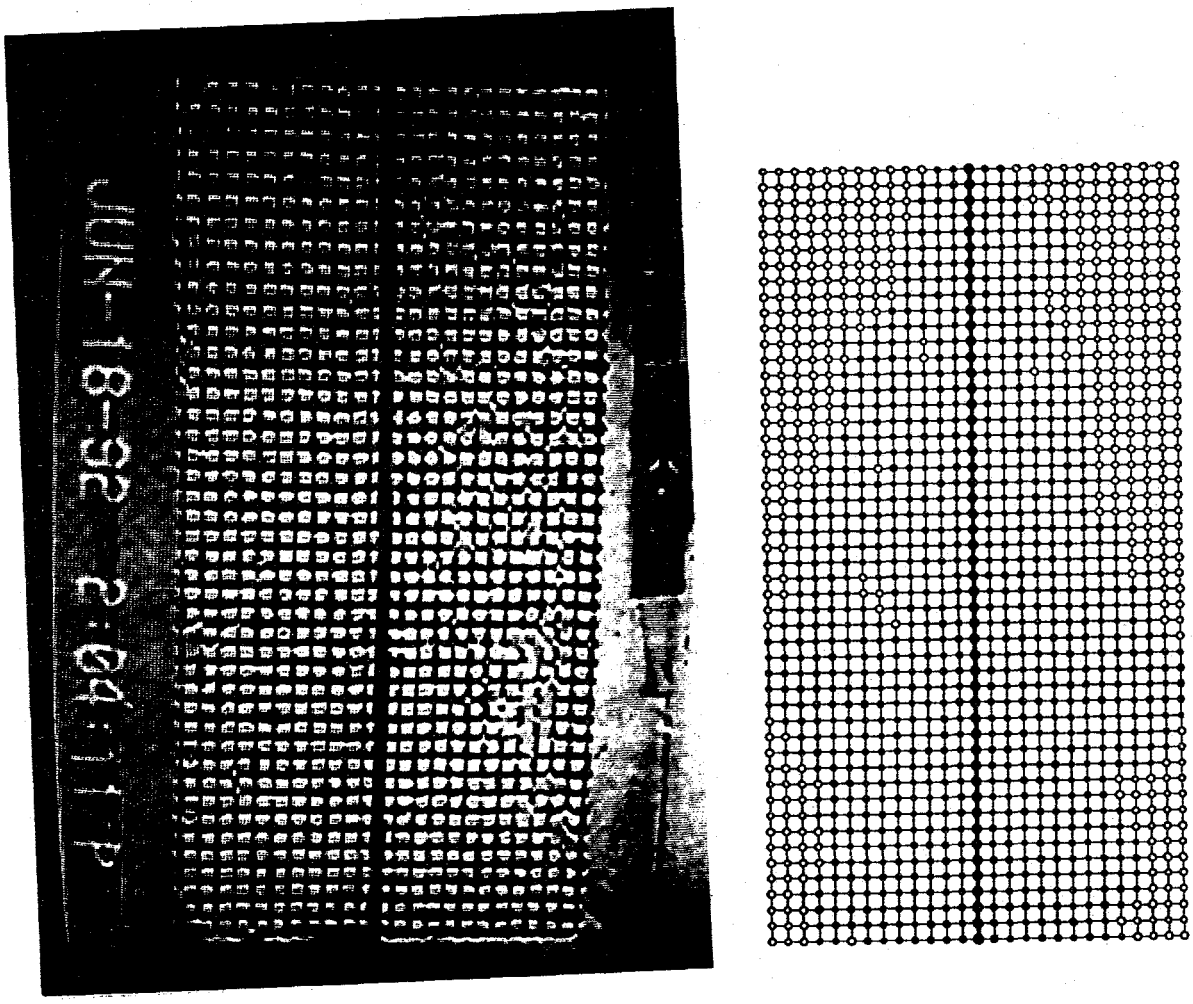

Figure 30: Comparison between experimental and numerical results for water-air, $Ca = 5.4 \times 10^{-4}$.

dominant mechanisms under this condition (Figure 31). The capillary number was next increased to 1.8×10^{-6}, and the results are shown in Figure 32. Now, in addition to film flow, we have pore filling mechanisms as well; however, the fracture is practically not invaded. Then, the simulation was run at $Ca = 5.4 \times 10^{-6}$ (Figure 33). In this case, the fracture starts to be invaded; however, at steady state, the full fracture penetration was arrested. This result is comparable to a previous set (Figure 29) at $Ca = 5.4 \times 10^{-5}$, where film flow did not take place. Because of the order of magnitude difference between the two results, this is supporting the fact that in the experiments a film flow mechanism did not exist. The final run is at a capillary number of 5.4×10^{-5}. At these conditions, pore filling is the dominant mechanism. This is similar to a previous set (Figure 30) at $Ca = 5.4 \times 10^{-4}$. Comparison between the two indicates that if there is film flow, the start of the fracture invasion and the competition between displacement fronts in the fracture and the matrix occur sooner.

In another set of simulations, the imbibition in the water-oil pair was studied. A network of size 60×20, with fractures in the side of the model is considered. Here, injection is through the entire inlet-face. The viscosity ratio is 100, while bond and pore radii of the fracture are five times larger to those in the matrix. The pore radius is ten times the bond radius. No film flow is assumed. The critical capillary number (when the front in the matrix and the fracture are the same) was 0.67×10^{-4} (Figure 35). The calculated value from equation (12) is 0.12×10^{-4}, which is a relatively good match despite the simplifications in deriving the formula. Then, the simulator was run for the same network, but with a bond radius one half of the previous. Now, the resulting critical capillary number becomes 0.75×10^{-6} (which is $\frac{1}{16}$ smaller of the previous). This is expected from Eq. (12), which shows that the cross section area and the matrix permeability are proportional to the second power of the bond radius. This indicates that the critical capillary number is proportional to matrix permeability. We also run the simulator for different lengths and viscosity ratios and found the critical capillary number to be inversely proportional to the length and viscosity ratio. This set of simulations confirmed the proposed relationship (Eq. 12) for the critical capillary number. Finally, the simulator was run for a different mobility ratio. Figure 36 shows the effect of viscosity ratio on both critical capillary numbers. At mobility ratio values smaller than one, the effect of the mobility ratio on the first critical capillary number is relatively small (Fig. 36a). At mobility ratio values higher than one, on the other hand, the slope obtained is close to 1 (Fig. 36b). This

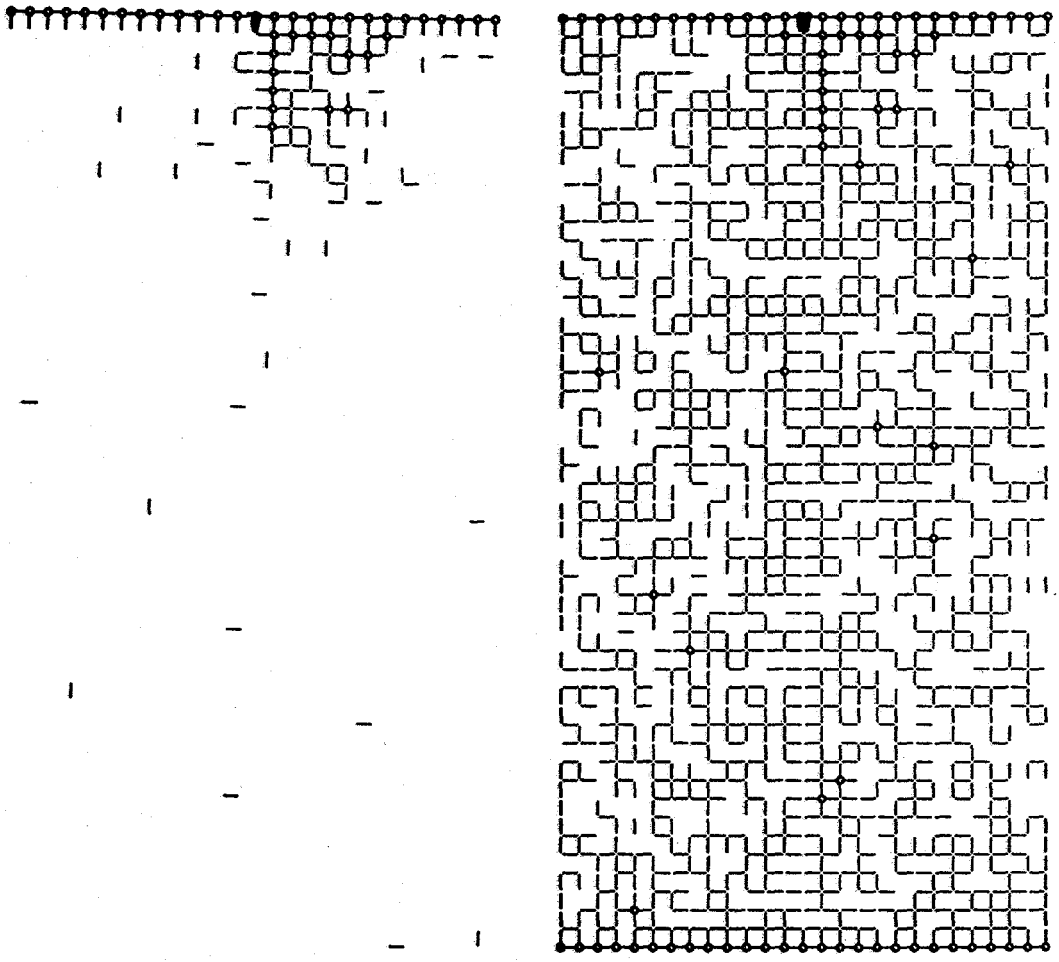

Figure 31: Numerical simulation of secondary imbibition (water-air) $Ca = 5.4 \times 10^{-8}$ (left: early time, right: steady state).

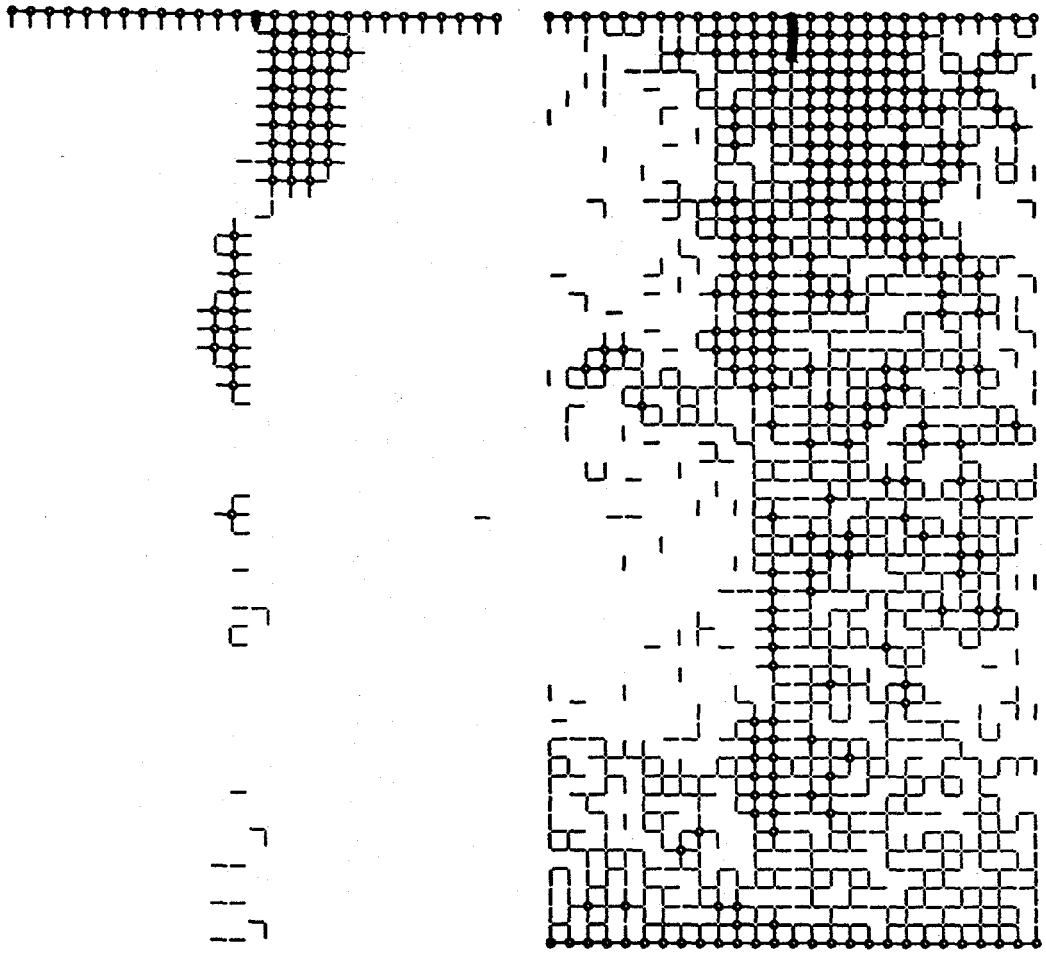

Figure 32: Numerical simulation of secondary imbibition (water-air) $Ca = 1.6 \times 10^{-6}$ (left: early time, right: steady state).

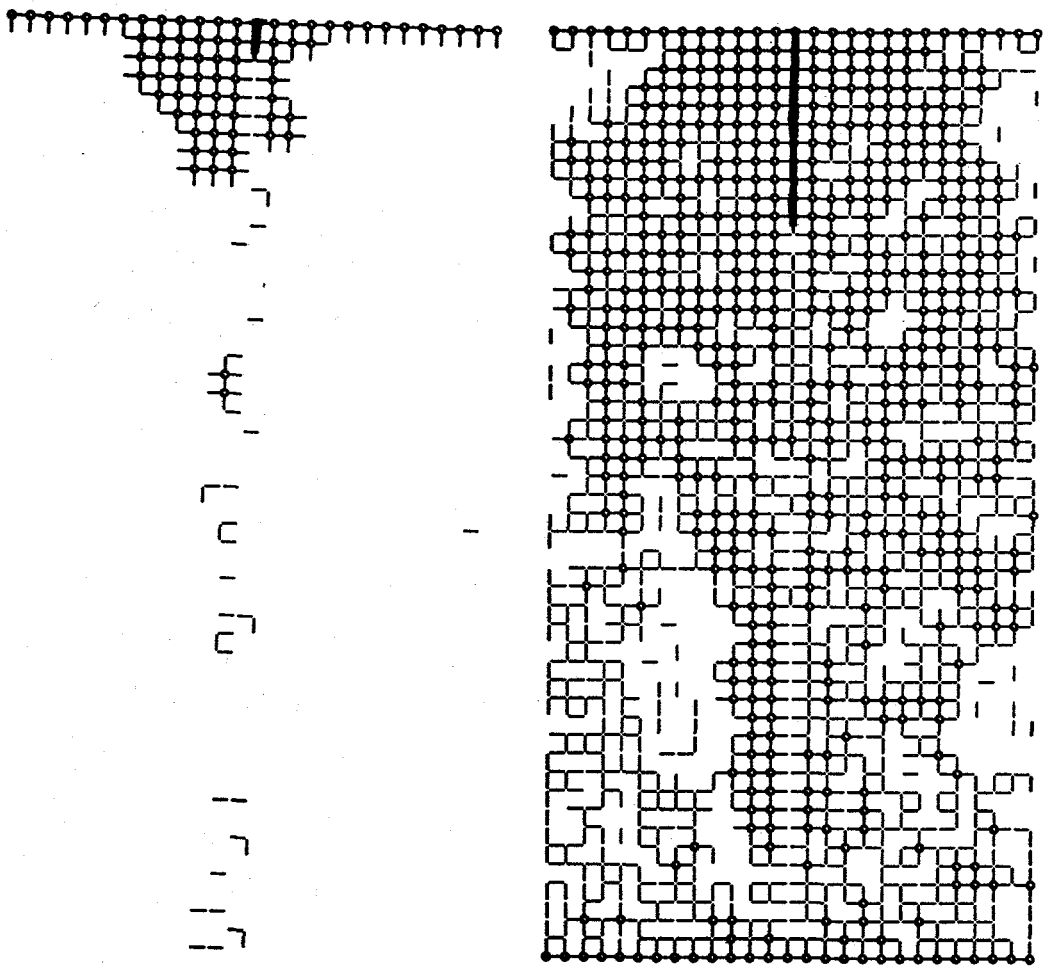

Figure 33: Numerical simulation of secondary imbibition (water-air) $Ca = 5.4 \times 10^{-6}$ (left: early time, right: steady state).

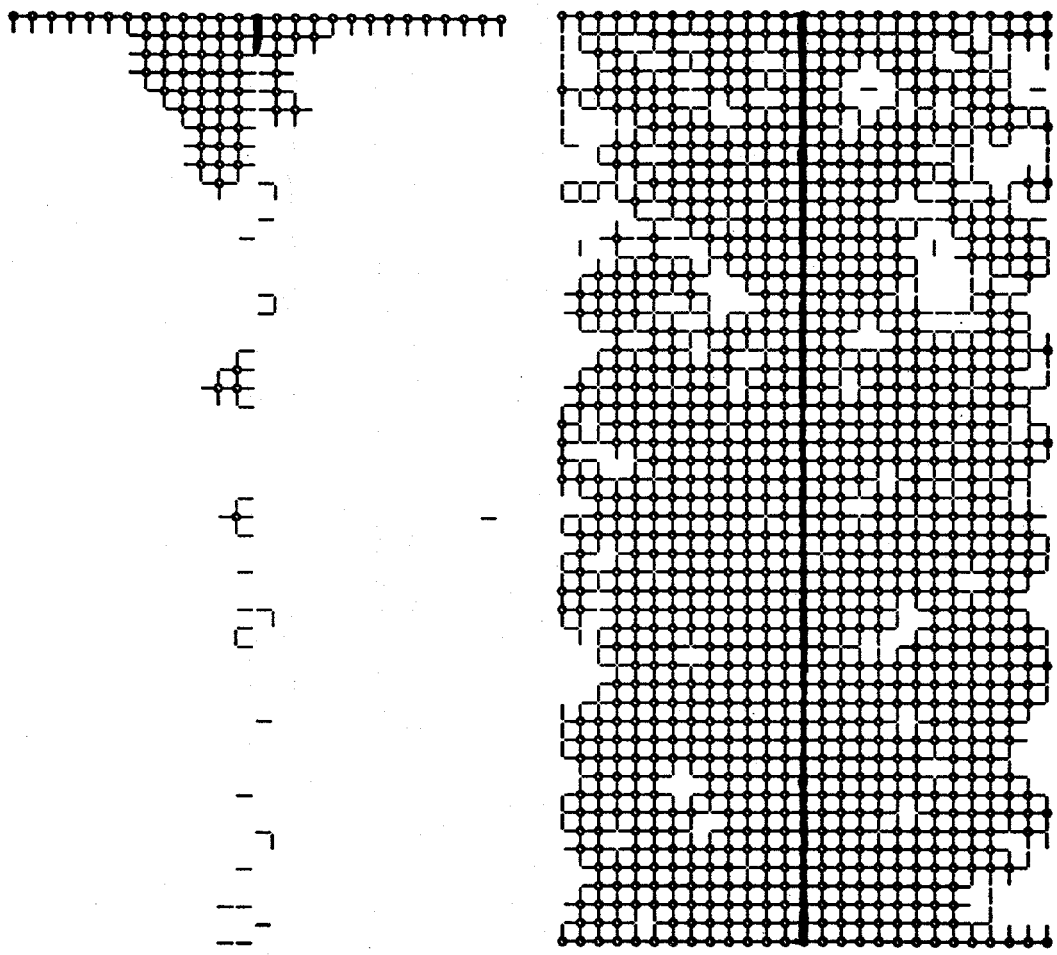

Figure 34: Numerical simulation of secondary imbibition (water-air) $Ca = 5.4 \times 10^{-5}$ (left: early time, right: steady state).

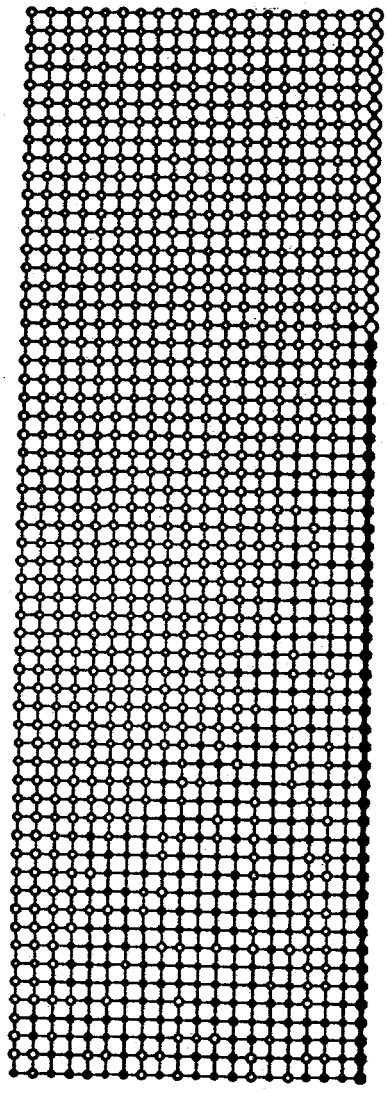

Figure 35: Numerical simulation of primary imbibition (water-air) $Ca = 0.67 \times 10^{-4}$, $M = 100$.

figures actually confirm the inverse proportionality of the first critical capillary number on mobility ratio, and show that the second capillary number is almost independent of the mobility ratio.

Finally, we simulated water-air free imbibition experiment. Now, the boundary condition was changed from constant flow rate to constant pressure, and we set both inlet and outlet pressure to be atmospheric. The primary imbibition simulator was used. Figure 37 shows four snapshots of the results obtained. Similar to the experiment, water moves into the matrix first and no substantial trapping is observed. When substantial matrix invasion develops, water starts to invade the fracture as well. We note that the water saturation versus time curve for this simulation is linear, the Aronofsy et al. [1] findings predict an exponential curve. The two, of course, are consistent at early times. Possible reasons for the discrepancy at later times are the assumption of no film flow and snap-off mechanisms in this simulation.

5 Conclusions

In this chapter, primary imbibition at the pore level was visualized. Two dominant mechanisms were identified are based on instantaneous invasion of a pore and its adjacent throat as the radius of curvature of meniscus increased, and another based on throat filling, when there is sufficient accumulation of water on the two walls of a throat. These mechanisms are comparable to the mechanism $I1$ and $I2$ defined by Lenormand et al. [16]. It was observed that at low capillary numbers the wetting fluid preferentially invaded the matrix. In secondary imbibition, a succession of rapid invasion jumps (snap-off events) also occurred along the existing water films. However, water films in displacement of the heavy oil are very thin, resulting in the lack of spontaneous imbibition. Free imbibition was also investigated. This process was shown to be a rapid invasion first of the matrix followed by a subsequent invasion of the fracture. Gravity effects on forced imbibition were also experimentally studied. With the use of a simplified theory, two critical capillary numbers were identified, one for the start of penetration in the fracture, and one for which the displacement front in the fracture is the same as that in the matrix. Expressions were developed for the former when the viscosity ratio was less than one, and for the latter when the viscosity ratio was greater than one. These values were well matched with experimental results and with results from numerical simulation. Pore network simulations matched the experimental

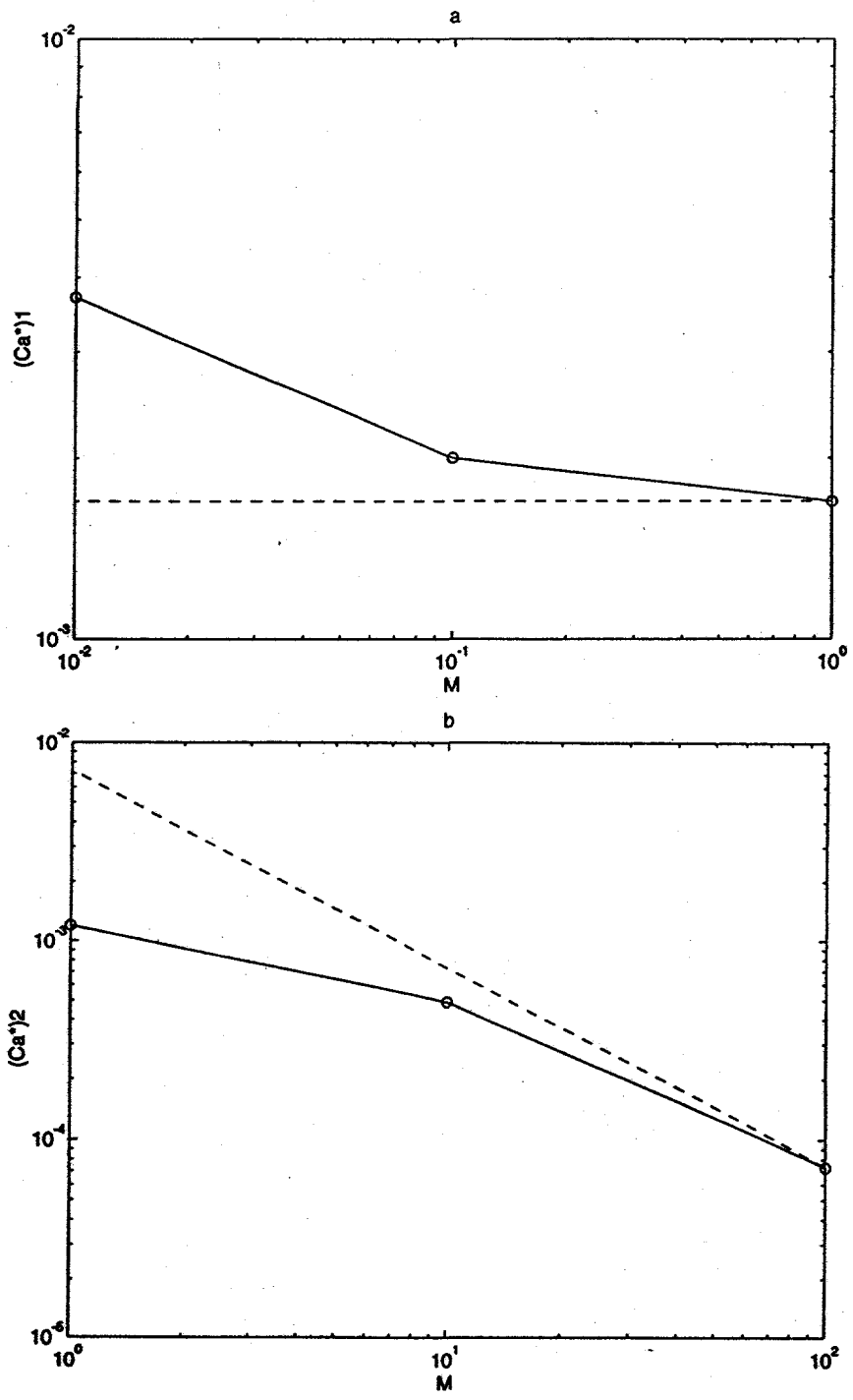

Figure 36: Dependence of the two critical capillary numbers (open circles) on the viscosity ratio for primary imbibition (the solid line is a guide to the eye). Theoretical predictions from Equations (7) and (11) are shown as dashed curves.

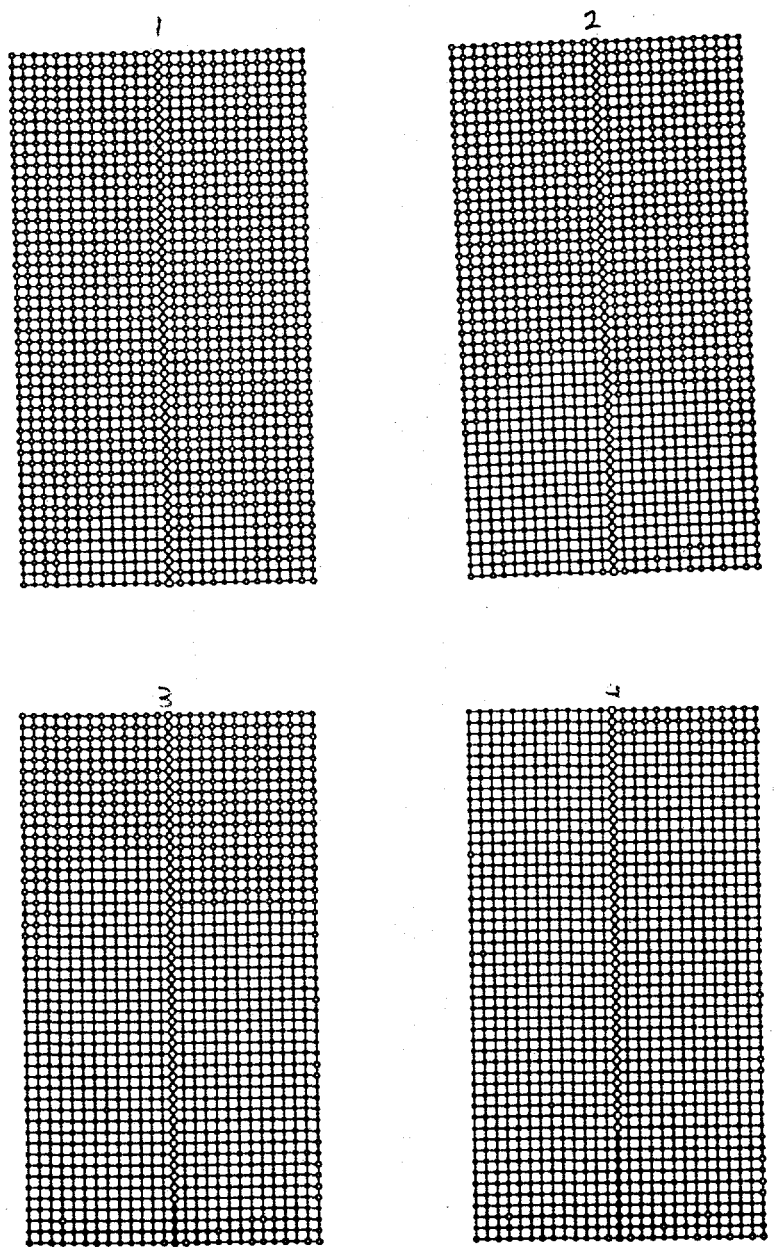

Figure 37: Numerical simulation of free imbibition (water-air). Four consecutive snapshots. Experimental results are shown in Figures 20- 23.

results and confirmed the two formulations of the critical capillary number. For $M \geq 1$, the critical capillary number is inversely proportional to the viscosity ratio while for $M \ll 1$ the effect of the viscosity ratio is small. Other than the viscosity ratio, the critical capillary numbers also depend on the geometric properties of the matrix. These critical capillary numbers allow us to identify three possible regimes:

1- There is no fracture penetration. In this case, the fracture actually does not play any role in the displacement process, and only the matrix relative permeability should be considered for the composite system.

2- The fracture front is ahead of the matrix front. Now, the matrix block will be surrounded by water and no imbibition occurs in the matrix. Therefore, the matrix relative permeability is of lesser importance in the composite behavior.

3- Fracture penetration exists and the fracture front is behind the matrix front. In this situation, a composite relative permeability consisting of both fracture and matrix exists.

References

[1] J.S. Aronofsky, L. Masse, and S.G. Natanson. *Trans, AIME*, 213:17, 1958.

[2] T. Babadagli. Ph.D. Dissertation, University of Southern California, 1993.

[3] M. Chaouche, N. Rakotomalala, D. Salin, B. Xu, and Y.C. Yortsos. Paper SPE 26658 presented at the 68th SPE Annual Technical Conference and Exhibition, Houston, Texas, 1993, also *Chem.Eng.Sci.* (in press), 1994.

[4] W.H. Chen, M.L. Wasserman, and R.E. Fitzmorris. Paper SPE 16008 presented at the 1986 SPE Symposium on Reservoir Simulation, San Antonio, February 1-4, 1987.

[5] F. F. Jr. Craig. *Monograph 3.* SPE, Richardson, TX, 1971.

[6] de Swaan. *SPEJ*, 18:117, 1978.

[7] A.S. Eka and I. Ershaghi. Paper SPE 10758, presented at the SPE California Regional Meeting, San Francisco, CA, 1982.

[8] M. Haghighi, B. Xu, and Y. C. Yortsos. *J. Colloid Interface Sci.* (in press), 1994.

[9] L.L. Handy. *Trans. AIME*, 219:75, 1960.

[10] L.L. Handy and P. Datta. *Chevron California Research Center Report*, 1964.

[11] T.B. Jensen. Ph.D. Dissertation, Univ. of Wyoming, 1991.

[12] A.J. Katz and A.H. Thompson. *Phys. Rev. B*, 34:8175, 1987.

[13] A. Labastie. Paper SPE 20515 presented at the 65th SPE Annual Meeting, New Orleans, LA, 1990.

[14] B.Y.Q. Lee and T.B.S. Tan. Paper SPE 16009 presented at the 1986 SPE Symposium on Reservoir Simulation, San Antonio, February 1-4, 1987.

[15] R. Lenormand. *J. Phys. C.:Condens. Matter*, 2:SA79, 1990.

[16] R. Lenormand, E. Touboul, and C. Zarcone. *J. Fluid Mech.*, 189:165, 1988.

[17] C.C. Mattax and J.R. Kyte. *SPEJ*, 2:177, 1962.

[18] M. Prats. *Thermal Recovery.* SPE, Richardson TX, 1982.

[19] R.H. Rossen and E.I. Shen. Paper SPE 16982 presented at the 62nd SPE Annual Meeting, Dallas, TX, 1987.

[20] A. M. Saidi. *Reservoir Engineering of Fractured Reservoirs: Fundamental and Practical Aspects.* Total Edition Presse, Paris, 1988.

[21] B. Xu. Ph.D. Dissertation, Univ. of Southern California, anticipated Dec. 1994.

☆U.S. GOVERNMENT PRINTING OFFICE: 1995 - 660-029/20038